Improving Navigation in GNSS-challenging Environments: Multi-UAS Cooperation and Generalized Dilution of Precision

Flavia Causa and Giancarmine Fasano, *IEEE Senior Member*

Abstract—This paper presents an approach to tackle navigation challenges for Unmanned Aircraft Systems flying under non nominal GNSS coverage. The concept used to improve navigation performance in these environments consists in using one or more cooperative platforms and relative sensing measurements (based on vision and/or ranging) to the navigation aid. The paper details the cooperative navigation filter which can exploit multiple cooperative platforms and multiple relative measurements, while also using partial GNSS information. The achievable navigation accuracy can be predicted using the concept of "generalized dilution of precision", which derives from applying the idea of dilution of precision to the mathematical structure of the cooperative navigation filter. Values and trends of generalized dilution of precision are discussed as a function of the relative geometry in common GNSS-challenging scenarios. Finally, navigation performance is assessed based on simulations and on multi-drone flight tests.

Index Terms—GNSS challenging environments; cooperative navigation; Multi GNSS constellation; generalized dilution of precision; camera and ranging measurements

I. Introduction

UNMANNED Aerial Vehicles (UAVs), born as military platforms, are nowadays widely used in many civil operations, such as mapping, aerial photography, search and rescue, package delivery, inspection. The increasing interest in the usage of small UAVs in daily life applications is due to their mobility, flexibility and relatively low cost [1]. Autonomy is the key feature to unleash UAV potential, allowing the final users to perform several missions while not requiring significant (or even any) piloting skills.

Reliable autonomous navigation is one of the main requirements for vehicle autonomy, since guidance and control commands (path tracking and decision making [2]), depend on navigation estimates. Kalman filters using inertial sensors (INS), Global Navigation Satellite System (GNSS) receivers, and magnetometers (MAG), are commonly used for navigation in open sky conditions.

Nevertheless, civil usage of UAVs often requires operating in low altitude environments, where the GNSS signal is not nominal due to multipath or signal absorption and obstruction by the surrounding obstacles, i.e. buildings, hills, bridges, vegetation. In these scenarios, usually referred to as GNSS challenging areas, GNSS signals cannot guarantee reliable position estimation [3], [4].

Several works addressed the problem of navigation in GNSS challenging areas by planning trajectories that minimize the positioning uncertainty (based on the covariance matrix of the state within the navigation filter) [5]–[8] and in general depend on the performance of the onboard sensors. References [9]–[12] developed techniques for detecting, removing, and mitigating the multipath affected measurements to improve the navigation performance, based on terrain maps, cooperation and/or on signal decoding and acquisition [13], [14]. Whilst, [15] controlled the error divergence by adding velocity constraints. These approaches bound the navigation error by optimizing the available measurements. However, navigation-aware planning is not always feasible, depending on the mission requirements. In addition, satellite pseudorange removal can lead to degraded dilution of precision (DOP) or even to the unavailability of positioning information if less than four satellites remain.

Therefore, a common solution to address the lack of GNSS satellites is using additional aiding information. Visual-based aiding has been extensively employed in this framework. References [16]–[21] used a visual/inertial approach to support localization when GPS signal is missing. This approach usually identified as Simultaneous Localization and Mapping (SLAM) aims at identifying landmarks and estimating their positioning along with that of the flying platform. Besides visual-based architectures, other approaches include opportunistic navigation [22] (e.g., based on phone signals [23]), exploitation of ground-based radio beacons [24], [25], or onboard Lidar [26] measurements. In spite of this research progress, safe and autonomous navigation in GNSS-challenging environments can still be considered as an open issue. In fact, each solution approach has limits and challenges. As an example, visual aided navigation can exhibit worse accuracy or fail in untextured or poorly textured environments, or in non-optimal illumination conditions. Furthermore, in general odometry approaches are aimed at estimating incremental motion, which allows them to reduce the rate of position error drift, but not to ensure bounded errors.

Cooperative navigation [27] also represents a promising strategy to improve navigation performance. It is based on a network of vehicles that share measurements and information to the navigation advantage [28], [29]. Different strategies have

This research was carried out in the frame of project "CREATEFORUAS", funded within Programme PRIN.

F. Causa and G. Fasano are with the Department of Industrial Engineering, University of Naples "Federico II", Naples, Italy. (e-mail: flavia.causa@unina.it, giancarmine.fasano@unina.it,)

been proposed in the open literature, which are based on relative range/angles measurements [28], [30] or on the observations of common ground areas by onboard optical sensors [27], [31]. Reference [32] uses a cooperative UGV to simulate an additional satellite to the aim of navigating a UAV under non nominal GNSS coverage. RF ranging measurement is acquired on board the UAV and used along with the precise position of the UGV, shared in the network. Trajectory optimization of the UGV has been discussed in [33]. A similar approach was used in [30] to perform canyon mapping. In this case a formation of two UAVs is used. The UAV at low altitude is equipped with high power LED, that allow the higher UAV (under nominal GNSS coverage) to estimate its 3D relative position with a camera.

The authors in [34] defined a more general approach, where one or more cooperative UAVs placed in nominal GNSS coverage, and named as "fathers", are demanded to support the flight of a UAV, called "son", in GNSS challenging environment. Differently from most of the work in the open literature [16]–[22], [24], [25], [30], the proposed approach does not assume GNSS availability as a binary input, or considers this source of measurement not available at all (GNSS-denied environments). Conversely, it tries to take the most advantage from the available GNSS information (from satellites in view), using tight integration of pseudorange measurements and compensating for the lack of accurate and reliable GNSS-based positioning information by cooperative measurements. Aiding provided by cooperative navigation can be tailored to GNSS coverage conditions and positioning accuracy needs. This allows having a bounded positioning error, also when a GNSS fix cannot be obtained (number of satellites lower than 4) [35]. The proposed approach can be actually integrated with single-vehicle-based navigation techniques that exploit exteroceptive sensors such as cameras or Lidars.

Reference [35] tested the proposed navigation strategy by analyzing the navigation performance of the son using different sensors, e.g. camera and/or RF ranging, as sources for estimating relative positioning among the platforms. To this aim, the concept of "generalized Dilution of Precision" (geDOP) was introduced. The generalized DOP is an extension of the concept of dilution of precision and allows estimating the position accuracy of the vehicle under non nominal GNSS coverage accounting for the GNSS observables of the visible satellites and the cooperative contribution. This concept can be used to estimate *a priori* the navigation performance of the "son", depending on the cooperative formation geometry, and therefore employed as path planning cost function [36] to define the trajectory of the father(s) that minimizes the navigation error of the son.

This paper contributes to this line of research providing the following innovative points:

- Introduction of a more complete formulation of the geDOP, which also accounts for son attitude uncertainty in positioning error estimation. This is needed when attitude/position cross-coupling effects exist, e.g. in the case relative sensing information is provided by camera(s) mounted on the son. In addition, cross-correlation of different sensing measurements, and actual father GNSS coverage and DOP conditions, are accounted for.
- Analysis of geDOP variation with multiple fathers.
- Use of multi-GNSS constellation, including GPS, Galileo and GLONASS.
- Assessment of model performance with simulated and experimental data in a wide set of scenarios.

The paper introduces the cooperative navigation concept in section II and describes the son state estimation filter in section III. The new expression for the generalized DOP is derived in section IV. Hence, simulation and experimental results are reported in section V.

II. Cooperative Navigation Concept

A conceptual scheme of the developed cooperative navigation concept is reported in Fig. 1, where fathers, reported in red, are required to be always in line of sight (LOS) with the son and outside the GNSS challenging area. Being under nominal GNSS coverage, father platforms can estimate with very high reliability their state (position, velocity and attitude) using a standard GNSS/INS/MAG powered navigation filter, and do not use cooperation support to improve their state estimation. On the contrary, cooperative (relative) measurements are used for the sake of son's navigation. Relative sensing can be carried out exploiting different sensing technologies. Ranging sensors, which can provide very accurate information, especially in the case ultra-wideband radio-frequency (RF) sensing technologies are considered (cm-level), have been extensively used in this framework [32]. On the other hand, cameras, commonly embarked on small UAVs, also represent a valid option, due to their low cost and small size, weight and power budget. Thanks to fast and accurate visual tracking algorithms, cameras can guarantee a very precise estimation of the line-of-sight (LOS) between cooperative aircraft (indeed, they can also provide ranging information using the paradigm of shape-based ranging [37], though the accuracy is strongly dependent on the actual range and the vehicle dimensions).

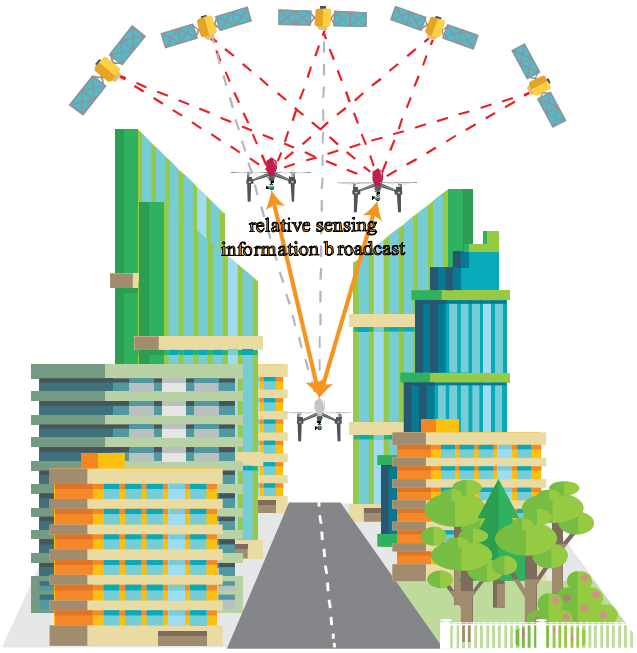

Fig. 1. Cooperative Navigation Concept. Son vehicle in grey, Father vehicles in red. Signals' raypath are depicted with dashed lines.

In the following, it will be assumed that ranging information is provided (only) by ad-hoc ranging sensors, though the developed algorithms and concepts are sensor-agnostic. Camera(s) can be installed either on board the son (son-to-father visual tracking) or the father (father-to-son visual tracking). If cooperative navigation is implemented in real time, the concept described in this paper requires the UAVs to share information among the network, e.g. fathers should share their position and eventual relative measurements, i.e. output of father-to-son visual-tracking. Thus, LOS link between the fathers and the son must be maintained during the flight in the challenging area not only to enable relative measurements, but also to ensure information broadcast. In theory, inter-UAV communications are not required if cooperative navigation is to be applied in post processing phase.

III. Navigation Filter

A tightly coupled Extended Kalman Filter (EKF) [38], whose scheme is depicted in Fig. 2, is used to estimate the son's navigation state. It includes 15 components which represent estimated error on vehicle absolute geodetic position $\mathbf{p}$ (composed by latitude l, longitude λ, and altitude h, in the WGS-84 ellipsoid), error on velocity $\mathbf{v}$ and attitude error vector $\boldsymbol{\rho}$ (both computed in local North East Down (NED) reference frame), errors on accelerometer and gyroscope biases, respectively $\delta\mathbf{b}_a$ and $\delta\mathbf{b}_g$, which are lumped together in vector $\delta\mathbf{b}$. $\delta\mathbf{b}_a$ and $\delta\mathbf{b}_g$ are 3×1 vectors including the 3 components of biases errors in son's body reference frame (BRF).

$$\delta\mathbf{x} = \begin{bmatrix} \delta\mathbf{p} \\ \delta\mathbf{v} \\ \boldsymbol{\rho} \\ \delta\mathbf{b} \end{bmatrix}; \quad \begin{aligned} \delta\mathbf{p} &= \begin{bmatrix} \delta l & \delta\lambda & \delta h \end{bmatrix}^T \\ \delta\mathbf{v} &= \begin{bmatrix} \delta v_n & \delta v_e & \delta v_d \end{bmatrix}^T \\ \boldsymbol{\rho} &= \begin{bmatrix} \varepsilon_n & \varepsilon_e & \varepsilon_d \end{bmatrix}^T \\ \delta\mathbf{b} &= \begin{bmatrix} \delta\mathbf{b}_a & \delta\mathbf{b}_g \end{bmatrix}^T \end{aligned} \tag{1}$$

While propagation is based on Inertial Measurement Unit (IMU) outputs and inertial navigation equations, measurements can be divided in two classes, i.e. cooperative (highlighted in blue in Fig. 2) and non-cooperative (i.e., single-vehicle-based, in grey) ones. GNSS measurements are the pseudoranges of the satellites in view of the receiver, whereas magnetometer outputs are the three components of the Earth magnetic field. When under non-nominal GNSS coverage, at least one cooperative measurement is needed to prevent filter divergence, or more in general to enhance navigation accuracy. The cooperative measurements depend on the sensor(s) embarked on the UAVs, and in general they include range and LOS angles. Relative measurements alone are not able to correctly upgrade the absolute position of the son, and must be complemented with the position of the j-th father in a fixed origin NED reference frame $\mathbf{r}_{f_j}^n$, broadcasted with its covariance to the cooperative network. It is assumed that, given the relatively short mission range and baselines among the flying platforms, definition of NED axes is independent of the actual point considered as origin.

Relative range represents the norm of the father-son position vector. As far as camera is concerned, in the case of son-to-father tracking, camera measurements (referred to as relative angles in Fig. 2) are azimuth and elevation of the father in the son's camera frame (CRF). Conversely, when the camera is mounted on the father, azimuth and elevation measured in father's CRF are transformed in NED, based on the estimate of father's attitude, and then broadcasted to the cooperative network. This choice is made to minimize the amount of information to be transferred to the son.

The measurement vector ($\delta\mathbf{y}$) is composed by residuals, estimated as the difference between the measured and the predicted values, i.e.:

$$\delta\mathbf{y} = \begin{bmatrix} \delta\mathbf{y}_{GNSS} \\ \hline \delta y_{mag} \\ \hline \delta\mathbf{y}_1 \\ \vdots \\ \delta\mathbf{y}_J \end{bmatrix} = \begin{bmatrix} \delta\Delta P_1 \\ \vdots \\ \delta\Delta P_M \\ \hline \varepsilon_{d,mag} \\ \hline \delta\mathbf{y}_1 \\ \vdots \\ \delta\mathbf{y}_J \end{bmatrix} \tag{2}$$

where $\delta\mathbf{y}_{GNSS}$ and δy_{mag} are the residuals associated to non-cooperative measurements, i.e. GNSS and magnetometer, respectively. Besides non cooperative measurements, the measurement vector includes J cooperative residual vectors, where $j = 1,\ldots,J$, and J is the number of available fathers. $\delta\mathbf{y}_j$ is the residual vector of the cooperative measurements associated to the j-th father.

The filter presented in this paper extends the one in [35] to the multi-GNSS constellation case. [35] uses the pivot satellite to cancel out the receiver clock error. Due to the need for removing from the measurements the inter-constellation bias [39] when dealing with multi-constellation receivers, a different pivot satellite is here chosen for each constellation. Therefore, the m-th component of the GNSS residual vector ($\delta\mathbf{y}_{GNSS}$) is given by $\delta\Delta P_m = \delta P_i^g - \delta P_{M_g}^g$, $m = 1,\ldots,M$. Where the pseudorange residual of the pivot satellite of the g-th constellation, i.e. $\delta P_{M_g}^g$, is subtracted from the pseudorange residuals of the i-th satellite of the g-th constellation, i.e δP_i^g. $i = 1,\ldots,M_g$-1 and M_g is the number of satellites belonging to the g-th constellation seen by the receiver.

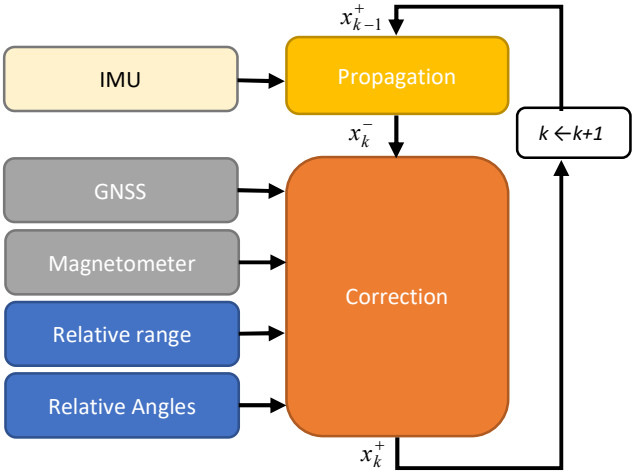

Fig. 2. EKF architecture. The input, i.e. sensor measurements can be classified as cooperative (blue) and single-vehicle-based (grey).

The total number of GNSS residuals, i.e. M can be estimated summing up the number of the satellites seen for each constellation and subtracting a measure (pivot) for each constellation. Therefore $M = \sum_{g=1}^{n_g} M_g - n_g$, being n_g the number of constellations that the receiver can track, $g = 1,\ldots,n_g$.

As far as magnetometer measurements are concerned, they are transformed in the scalar heading residual δy_{mag}, thanks to the roll and pitch estimates, whose error can be reasonably assumed to be bounded.

The residual vector of the cooperative measurements associated to the j-th father ($\delta\mathbf{y}_j$) includes, in general range ($\delta y_{j,R}$), son-to-father $\left(\delta\mathbf{y}_{j,EO}^{s\to f}\right)$, and father-to-son $\left(\delta\mathbf{y}_{j,EO}^{f\to s}\right)$ visual tracking residuals, i.e.:

$$\delta y_{j,R} = \delta r_j$$
$$\delta\mathbf{y}_j = \begin{bmatrix} \delta y_{j,R} \\ \delta\mathbf{y}_{j,EO}^{s\to f} \\ \delta\mathbf{y}_{j,EO}^{f\to s} \end{bmatrix};\ \delta\mathbf{y}_{j,EO}^{s\to f} = \begin{bmatrix} \delta Az_{s\to f_j}^{c_s} \\ \delta El_{s\to f_j}^{c_s} \end{bmatrix} \qquad (3)$$
$$\delta\mathbf{y}_{j,EO}^{f\to s} = \begin{bmatrix} \delta Az_{f_j\to s}^{n} \\ \delta El_{f_j\to s}^{n} \end{bmatrix}$$

where $\delta y_{j,R} = \delta r_j$ is the residual of the distance between the son and the j-th father. Whereas, camera measurements include azimuth Az and elevation El. The pedices $s\to f_j$ or $f_j\to s$ indicates whether son-to-father or father-to-son measurement is considered, respectively. The apices c_s and n indicate respectively the son CRF and the NED frame where azimuth and elevation are defined, depending on which platform embarks the camera.

The navigation filter works on the basis of a prediction-correction scheme. Prediction is carried out following the standard equations reported in [38] and exploiting information from the inertial sensors. The filter correction or measurement equation relates the measurement residual vector ($\delta\mathbf{y}$) to the state ($\delta\mathbf{x}$), and is:

$$\delta\mathbf{y} = H\delta\mathbf{x} + \mathbf{w} \qquad (4)$$

where H indicates the measurement matrix and $\mathbf{w}$ is the noise associated to the measurement vector with covariance R.

The measurement matrix H can be written as:

$$\delta\mathbf{y} = \begin{bmatrix} \delta\mathbf{y}_{GNSS} \\ \hline \delta\mathbf{y}_{mag} \\ \hline \delta\mathbf{y}_1 \\ \vdots \\ \delta\mathbf{y}_J \end{bmatrix} = \underbrace{\left[\begin{array}{cccc} H_{GNSS\mathbf{p}} & 0_{m\times 3} & 0_{m\times 3} & 0_{m\times 6} \\ \hline 0_{1\times 3} & 0_{1\times 3} & H_{mag\boldsymbol{\rho}} & 0_{1\times 6} \\ \hline \multicolumn{4}{c}{H_1} \\ \multicolumn{4}{c}{\vdots} \\ \multicolumn{4}{c}{H_J} \end{array}\right]}_{H} \begin{bmatrix} \delta\mathbf{p} \\ \delta\mathbf{v} \\ \boldsymbol{\rho} \\ \delta\mathbf{b} \end{bmatrix} \qquad (5)$$

H_j indicates the measurement matrix associated to the j-th father, that will be detailed in section III.B. Whereas the symbol "$H_{l\mathbf{z}}$" represents the submatrix of matrix H connecting the measurement of sensor "l", with the "$\mathbf{z}$" part of the state vector (that can be position $\mathbf{p}$, velocity $\mathbf{v}$, attitude $\boldsymbol{\rho}$ or bias $\mathbf{b}$). Therefore, $H_{GNSS\mathbf{p}}$ and $H_{mag\boldsymbol{\rho}}$ are, respectively, the matrices defining the dependence of the GNSS residuals on position error and the dependence of magnetometer residual on attitude error, as follows:

$$H_{GNSS\mathbf{p}} = \left[\begin{array}{c} \frac{\partial P_1^1}{\partial\mathbf{p}} - \frac{\partial P_{M_1}^1}{\partial\mathbf{p}} \\ \vdots \\ \frac{\partial P_{M_1-1}^1}{\partial\mathbf{p}} - \frac{\partial P_{M_1}^1}{\partial\mathbf{p}} \\ \hline \vdots \\ \hline \frac{\partial P_1^{n_g}}{\partial\mathbf{p}} - \frac{\partial P_{M_{n_g}}^{n_g}}{\partial\mathbf{p}} \\ \vdots \\ \frac{\partial P_{M_{n_g}-1}^{n_g}}{\partial\mathbf{p}} - \frac{\partial P_{M_{n_g}}^{n_g}}{\partial\mathbf{p}} \end{array}\right];\ H_{mag\boldsymbol{\rho}} = \begin{bmatrix} 0 & 0 & 1 \end{bmatrix} \qquad (6)$$

P_i^g indicates the pseudorange of the i-th satellite of g-th constellation. The matrix explicitly defines the subtraction of the pivot satellite chosen for each constellation, i.e. M_g. $\partial P_i^g / \partial\mathbf{p}$ is the derivative of the pseudorange with respect to the three components of the geodetic position, whose derivation is not reported herein for the sake of brevity. The interested reader is referred to [38].

As far as the measurement covariance matrix R is concerned, it is given by:

$$R = \begin{bmatrix} R_{GNSS} & 0_{M\times 1} & 0_{M\times 5J} \\ 0_{1\times M} & R_{mag} & 0_{1\times 5J} \\ 0_{5J\times M} & 0_{5J\times 1} & R_c \end{bmatrix}$$
$$R_c = \begin{bmatrix} R_1 & \cdots & 0_{5\times 5} \\ \vdots & \ddots & \vdots \\ 0_{5\times 5} & \cdots & R_J \end{bmatrix} \qquad (7)$$

where R_c is the cooperative covariance matrix obtained by diagonally concatenating the covariance matrices of the J fathers. The covariance matrix of the j-th father, i.e. R_j (j=1,…,J), is derived in section III.C. R_{mag} is the magnetometer covariance matrix equal to the magnetometer heading variance $R_{mag} = \sigma_{\psi_{mag}}^2$, and R_{GNSS} is the covariance matrix of the GNSS measurement depending on the standard deviation of pseudorange errors, σ_{Pr},, assumed to be equal for each satellite:

$$R_{GNSS} = \left(\mathbf{I}_M + \begin{bmatrix} \mathbf{1}_{M_1-1} & 0 & 0 \\ 0 & \ddots & 0 \\ 0 & 0 & \mathbf{1}_{M_{n_g}-1} \end{bmatrix} \right) \sigma_{Pr}^2 \qquad (8)$$

where $\mathbf{1}_a$ is the matrix containing all ones of size $a\times a$, whereas $\mathbf{I}_a$ is the $a\times a$ identity matrix.

A. *Measurement equations for cooperative aiding*

Following equation (4), the linearized form of the measurement equation of the sensor "*l*" is $\delta\mathbf{y}_l = H_l\delta\mathbf{x} + \mathbf{w}_l$. This section is in charge of defining the measurement equation for each cooperative measurement.

Although the geodetic coordinates are indicated in equation (1) by the symbol $\mathbf{p}$, the derivation reported in the following requires operating with the position vectors in Cartesian coordinates. The position vector of the platform *i* in the frame *a* is reported as $\mathbf{r}_i^a$. Whereas, the rotation matrix from the frame *a* to the frame *b* is indicated with C_a^b, thus $\mathbf{r}_i^b = C_a^b\mathbf{r}_i^a$. Specifically NED, Earth Fixed Earth Centered (ECEF), body (BRF) and camera frame (CRF) are accounted for in this work, which are identified with the letters *n*, *e*, b_i and c_i. The pedex *i* indicates for the body and the camera frame the platform to which they are referred to. For the sake of completeness, Fig. 3 shows the NED frame and the body and camera frame for the son platform, indicated as b_s and c_s, respectively. The *h*-th axis of the a_s frame is indicated as $a_s(h)$.

In the following, σ indicates the standard deviation (STD) value associated to a scalar quantity. Ranging and camera (angular) error STDs are identified with σ_R and σ_{cam}, respectively. When a vector $\mathbf{a}$ is accounted for, $\Sigma_\mathbf{a}$ indicates a diagonal matrix whose elements correspond to the STD of each component of $\mathbf{a}$. The error of the quantity α, which could be either a vector or a scalar, is indicated with $\delta\alpha$, and $\partial\alpha/\partial\mathbf{a}$ is the derivative of that quantity with respect to the vector $\mathbf{a}$.

1) *Son-to-father visual tracking*

The two measurements residuals of the camera for the *j*-th father, i.e. azimuth and elevation, can be estimated as a function of the relative position between the *j*-th father's center of mass (CoM) and the origin of son's CRF. This relative position vector, termed $\mathbf{r}_{s\to f_j}$ and expressed in NED is:

$$\mathbf{r}^n_{s\to f_j} = \mathbf{r}^n_{f_j} - \mathbf{r}^n_s - \mathbf{r}^n_{c,s} \tag{9}$$

Where $\mathbf{r}_{fi}$ and $\mathbf{r}_s$ are the CoM positions for the *j*-th father and the son, whilst $\mathbf{r}_{c,s}$ is the vector from son's CoM to the origin of its CRF, see Fig. 3. All these vectors are expressed in NED in eq. (9) as indicated by the apex *n*. The error on a generic vector estimated in ECEF can be converted in the error in NED frame with:

$$\delta\mathbf{r}^n = C_e^n\delta\mathbf{r}^e - \delta C_e^n\left(\mathbf{r}^e - \mathbf{r}_o^e\right) \tag{10}$$

This is obtained because the NED coordinates of a point $\mathbf{r}^n$ are related to its ECEF coordinates $\mathbf{r}^e$ through the position in ECEF of the origin of the NED frame $\mathbf{r}_o^e$, i.e. $\mathbf{r}^n = C_e^n\left(\mathbf{r}^e - \mathbf{r}_o^e\right)$.

Using the error form of eq. (9) and substituting $\delta\mathbf{r}_s^n$ with eq. (10), yields:

$$\delta\mathbf{r}^n_{s\to f_j} = \delta\mathbf{r}^n_{f_j} - C_e^n\delta\mathbf{r}_s^e - \delta\mathbf{r}^n_{c,s} - \delta C_e^n\left(\mathbf{r}_o^e - \mathbf{r}_s^e\right) \tag{11}$$

δC_e^n is the error in estimating the rotation from ECEF to NED [38]. The matrix depends on the error on the latitude and longitude of the NED frame origin, which is zero, being the origin of the NED frame fixed and correctly known.

Hence, using the rotation between NED and son's BRF, whose error depends on the attitude error $\boldsymbol{\rho}$, eq. (11) becomes:

$$\delta\mathbf{r}^n_{s\to f_j} = \delta\mathbf{r}^n_{f_j} - C_e^n\delta\mathbf{r}_s^e + \left[C_{b_s}^n\mathbf{r}^{b_s}_{c,s}\times\right]\boldsymbol{\rho} \tag{12}$$

$\mathbf{r}_{c,s}$ expressed in son's BRF has been reported with apex b_s. The operator $[\square\times]$ returns the skew-symmetric matrix.

The position error of the son in ECEF $\delta\mathbf{r}_s^e$ can be expressed as a function of the geodetic position error $\delta\mathbf{p}$, and eq. (12) becomes:

$$\delta\mathbf{r}^n_{s\to f_j} = \delta\mathbf{r}^n_{f_j} - C_e^n\frac{\partial\mathbf{r}_s^e}{\partial\mathbf{p}}\delta\mathbf{p} + \left[C_{b_s}^n\mathbf{r}^{b_s}_{c,s}\times\right]\boldsymbol{\rho} \tag{13}$$

Transforming this expression in son's CRF, and expressing relative position in terms of angular measurements [34], [35], the measurement residual equation of the camera, when mounted on the son is:

$$\delta\xi = \frac{\partial\xi}{\partial\mathbf{p}}\delta\mathbf{p} + \frac{\partial\xi}{\partial\mathbf{r}^n_{f_j}}\delta\mathbf{r}^n_{f_j} + \frac{\partial\xi}{\partial\boldsymbol{\rho}}\boldsymbol{\rho} + \delta_{cam}$$

$$\frac{\partial\xi}{\partial\mathbf{p}} = -\frac{\partial\xi}{\partial\mathbf{r}^{c_s}_{s\to f_j}}C_{b_s}^{c_s}C_n^{b_s}C_e^n\frac{\partial\mathbf{r}_s^e}{\partial\mathbf{p}};\ \frac{\partial\xi}{\partial\mathbf{r}^n_{f_j}} = \frac{\partial\xi}{\partial\mathbf{r}^{c_s}_{s\to f_j}}C_{b_s}^{c_s}C_n^{b_s} \tag{14}$$

$$\frac{\partial\xi}{\partial\boldsymbol{\rho}} = \frac{\partial\xi}{\partial\mathbf{r}^{c_s}_{s\to f_j}}C_{b_s}^{c_s}C_n^{b_s}\left[\left(\mathbf{r}^n_{f_j} - \mathbf{r}^n_s\right)\times\right]$$

where ξ is either $El^{c_s}_{s\to f_j}$ or $Az^{c_s}_{s\to f_j}$ and δ_{cam} is the visual tracking error that has a standard deviation (STD) σ_{cam} of the order of the camera Instantaneous Field of View (IFOV).

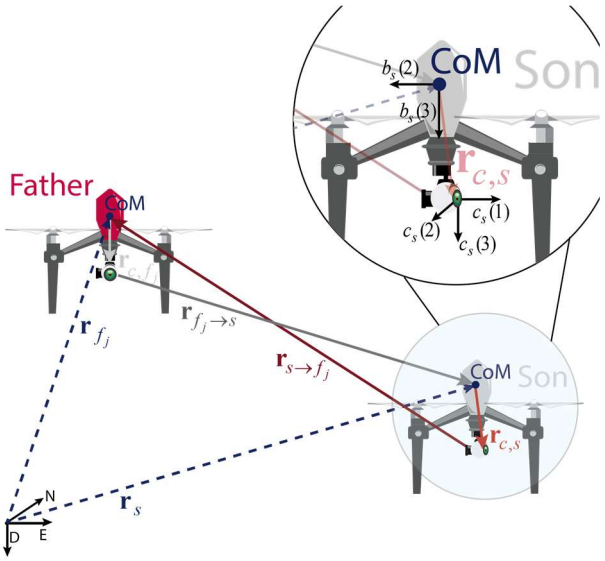

Fig. 3. Father to son geometry and camera measurements. Fixed origin NED frame and son's body (b_s) and camera (c_s) frame are reported. Body frame has its origin in the center of mass (CoM) of the platform. $b_s(h)$ and $c_s(h)$ indicate the *h*-th axis of b_s or c_s frame, respectively. The first axis of the son's body frame has not been reported for the sake of clarity assuming it is pointed towards the reader.

The son's BRF to son's CRF rotation matrix, i.e. $C_{b_s}^{c_s}$, can be assumed as constant for strapdown installations (which is the case considered in both simulations and flight experiments in this paper), and there exist several techniques for off-line calibration. In the case of gimbaled installations, it continuously changes and can be estimated in real time combining off-line calibration and real time gimbal telemetry (i.e., gimbal rotation angles).

2) Father-to-son visual tracking

The measurement equation for the camera mounted on the father is derived in analogy with the previous section. The *j*-th father's camera measures the Azimuth and the Elevation in the father's camera frame, indicated with apex c_{fj}. To reduce the amount of information to be shared in the cooperative network, father's camera measurements ($El_{f_j\to s}^{c_{f_j}}$ and $Az_{f_j\to s}^{c_{f_j}}$) are converted in Azimuth and Elevation in the NED frame ($El_{f_j\to s}^{n}$ and $Az_{f_j\to s}^{n}$) thanks to the following formula:

$$\mathbf{u}_{f_j\to s}^{n}=C_{b_{f_j}}^{n}C_{c_{f_j}}^{b_{f_j}}\begin{bmatrix}\cos El_{f_j\to s}^{c_{f_j}}\cos Az_{f_j\to s}^{c_{f_j}}\\ \cos El_{f_j\to s}^{c_{f_j}}\sin Az_{f_j\to s}^{c_{f_j}}\\ -\sin El_{f_j\to s}^{c_{f_j}}\end{bmatrix} \tag{15}$$

$$Az_{f_j\to s}^{n}=\operatorname{atan}\left(\mathbf{u}_{f_j\to s}^{n}(2)\Big/\mathbf{u}_{f_j\to s}^{n}(1)\right);El_{f_j\to s}^{n}=-\operatorname{asin}\left(\mathbf{u}_{f_j\to s}^{n}(3)\right)$$

where $\mathbf{u}_{f_j\to s}^{n}$ is the unit vector originated at father's camera that points towards the son CoM, whose *h*-th component is $\mathbf{u}_{f_j\to s}^{n}(h)$. The error equation associated to eq. (15), allows converting the angular uncertainty of the camera measurement, i.e. δ_{cam}, in NED, i.e.:

$$\Delta\chi^{n}=\frac{\partial\chi^{n}}{\partial\mathbf{u}_{f_j\to s}^{n}}C_{c_{f_j}}^{n}\frac{\partial\mathbf{u}_{f_j\to s}^{c_{f_j}}}{\partial\chi^{c_{f_j}}}\delta_{cam}-\frac{\partial\chi^{n}}{\partial\mathbf{u}_{f_j\to s}^{n}}\left[\mathbf{u}_{f_j\to s}^{n}\times\right]\boldsymbol{\rho}_{f_j} \tag{16}$$

where χ could be either $El_{f_j\to s}$ or $Az_{f_j\to s}$. In eq. (16), their representation in NED or father camera frame is indicated either with apex *n* or c_{fi} respectively. $\boldsymbol{\rho}_{fj}$ is the attitude error of the father.

In analogy with eq. (13), one can find an equation that connects the error on the vector between father's camera and son CoM, i.e. $\delta\mathbf{r}_{f_j\to s}$ to $\delta\mathbf{p}$. Expressed in NED, it is:

$$\delta\mathbf{r}_{f_j\to s}^{n}=C_{e}^{n}\frac{\partial\mathbf{r}_{s}^{e}}{\partial\mathbf{p}}\delta\mathbf{p}-\delta\mathbf{r}_{f_j}^{n}+\left[C_{b_{f_j}}^{n}\mathbf{r}_{c,f_j}^{b_{f_j}}\times\right]\boldsymbol{\rho}_{f_j} \tag{17}$$

where $\mathbf{r}_{c,f_j}^{b_{f_j}}$ is the position of the father camera in father's BRF, see Fig. 3. The measurement residual equation for father-to-son visual tracking is:

$$\delta\chi^{n}=\frac{\partial\chi^{n}}{\partial\mathbf{p}}\delta\mathbf{p}+\frac{\partial\chi^{n}}{\partial\mathbf{r}_{f_j}^{n}}\delta\mathbf{r}_{f_j}^{n}+\frac{\partial\chi^{n}}{\partial\boldsymbol{\rho}_{f_j}}\boldsymbol{\rho}_{f_j}+\Delta\chi^{n}$$

$$\frac{\partial\chi^{n}}{\partial\mathbf{p}}=\frac{\partial\chi^{n}}{\partial\mathbf{r}_{f_j\to s}^{n}}C_{e}^{n}\frac{\partial\mathbf{r}_{s}^{e}}{\partial\mathbf{p}} \tag{18}$$

$$\frac{\partial\chi^{n}}{\partial\boldsymbol{\rho}_{f_j}}=\frac{\partial\chi^{n}}{\partial\mathbf{r}_{f_j\to s}^{n}}\left[C_{b_{f_j}}^{n}\mathbf{r}_{c,f_j}^{b_{f_j}}\times\right];\frac{\partial\chi^{n}}{\partial\mathbf{r}_{f_j}^{n}}=-\frac{\partial\chi^{n}}{\partial\mathbf{r}_{f_j\to s}^{n}}$$

3) Ranging

The ranging measurement instrument is aimed at estimating the norm of the distance between the son and the supporting fathers. Using the same approaches described above, the corresponding measurement equation can be written as

$$\delta r_j=\frac{\partial r_j}{\partial\mathbf{p}}\delta\mathbf{p}+\frac{\partial r_j}{\partial\mathbf{r}_{f_j}^{n}}\delta\mathbf{r}_{f_j}^{n}+\delta_R \tag{19}$$

where δ_R is the error of the ranging measurement. This equation does not consider the lever arm term of ranging instrument.

B. Measurement Matrix for cooperative aiding

The cooperative measurement matrix for the *j*-th father can be obtained by considering only the state dependent terms in equations (14), (18) and (19), and is:

$$H_j=\begin{bmatrix}\overbrace{H_{j,R\mathbf{p}}}^{H_{j\mathbf{p}}} & 0_{1\times3} & \overbrace{0_{1\times3}}^{H_{j\boldsymbol{\rho}}} & 0_{1\times6}\\ H_{j,EO\mathbf{p}}^{s\to f} & 0_{2\times3} & H_{j,EO\boldsymbol{\rho}}^{s\to f} & 0_{2\times6}\\ H_{j,EO\mathbf{p}}^{f\to s} & 0_{2\times3} & 0_{2\times3} & 0_{2\times6}\end{bmatrix}$$

$$H_{j,R\mathbf{p}}=\frac{\partial r_j}{\partial\mathbf{p}}$$

$$H_{j,EO\mathbf{p}}^{s\to f}=\begin{bmatrix}\dfrac{\partial Az_{s\to f_j}^{c_s}}{\partial\mathbf{p}}\\ \dfrac{\partial El_{s\to f_j}^{c_s}}{\partial\mathbf{p}}\end{bmatrix};H_{j,EO\boldsymbol{\rho}}^{s\to f}=\begin{bmatrix}\dfrac{\partial Az_{s\to f_j}^{c_s}}{\partial\boldsymbol{\rho}}\\ \dfrac{\partial El_{s\to f_j}^{c_s}}{\partial\boldsymbol{\rho}}\end{bmatrix}$$

$$H_{j,EO\mathbf{p}}^{f\to s}=\begin{bmatrix}\dfrac{\partial Az_{f_j\to s}^{n}}{\partial\mathbf{p}}\\ \dfrac{\partial El_{f_j\to s}^{n}}{\partial\mathbf{p}}\end{bmatrix} \tag{20}$$

Equation (20) highlights the dependency of the cooperative measurement on son attitude only in the case the camera is mounted on the son. In the other cases, i.e. father-to-son visual tracking and ranging, the aiding measurements only contribute to positioning.

C. Covariance matrices for cooperative aiding

Section III.A reported measurement equations for the different cooperative measurements. Based on equations (14), (18), (19), the corresponding expressions for measurement covariance can be derived. To this aim, the part of the measurement equations that does not depend on the state vector is lumped in the term $\delta\tilde{\mathbf{y}}_j$, i.e.

$$\delta\tilde{\mathbf{y}}_j = \begin{bmatrix} \dfrac{\partial r_j}{\partial \mathbf{r}_f^n}\delta\mathbf{r}_{f_j}^n + \delta_R \\ \hline \dfrac{\partial Az_{s\to f_j}^{c_s}}{\partial \mathbf{r}_{f_j}^n}\delta\mathbf{r}_{f_j}^n + \delta_{cam} \\ \dfrac{\partial El_{s\to f_j}^{c_s}}{\partial \mathbf{r}_{f_j}^n}\delta\mathbf{r}_{f_j}^n + \delta_{cam} \\ \hline \dfrac{\partial Az_{f_j\to s}^n}{\partial \mathbf{r}_{f_j}^n}\delta\mathbf{r}_{f_j}^n + \dfrac{\partial Az_{f_j\to s}^n}{\partial \boldsymbol{\rho}_{f_j}}\boldsymbol{\rho}_{f_j} + \Delta Az_{f_j\to s}^n \\ \dfrac{\partial El_{f_j\to s}^n}{\partial \mathbf{r}_{f_j}^n}\delta\mathbf{r}_{f_j}^n + \dfrac{\partial El_{f_j\to s}^n}{\partial \boldsymbol{\rho}_{f_j}}\boldsymbol{\rho}_{f_j} + \Delta El_{f_j\to s}^n \end{bmatrix} \quad (21)$$

The covariance matrix relevant to cooperation with the j-th father is:

$$R_j = \left[\begin{array}{c|cc|cc} \sigma_R^2 & 0 & 0 & 0 & 0 \\ \hline 0 & \sigma_{cam}^2 & 0 & 0 & 0 \\ 0 & 0 & \sigma_{cam}^2 & 0 & 0 \\ \hline 0 & 0 & 0 & \multicolumn{2}{c}{\multirow{2}{*}{$R_{j,EO}^{f\to s}$}} \\ 0 & 0 & 0 & & \end{array}\right] + R_{cross} \quad (22)$$

The cooperative measurements are correlated by R_{cross}, which includes only the terms connected to the father positioning error (which influence all the measurements thus generating the cross-correlation among them) and is given by:

$$R_{cross} = \frac{\partial\tilde{\mathbf{y}}_j}{\partial\mathbf{r}_{f_j}^n}\Sigma_{\mathbf{r}_{f_j}^n}^2\left(\frac{\partial\tilde{\mathbf{y}}_j}{\partial\mathbf{r}_{f_j}^n}\right)^T \quad (23)$$

where $\Sigma_{\mathbf{r}_{f_j}^n}$ is a diagonal matrix including the three components of the standard deviation (STD) of father positioning error in NED, and

$$\frac{\partial\tilde{\mathbf{y}}_j}{\partial\mathbf{r}_{f_j}^n} = \left[\begin{array}{c|cc|cc} \dfrac{\partial r_j}{\partial\mathbf{r}_{f_j}^n} & \dfrac{\partial Az_{s\to f_j}^{c_s}}{\partial\mathbf{r}_{f_j}^n} & \dfrac{\partial El_{s\to f_j}^{c_s}}{\partial\mathbf{r}_{f_j}^n} & \dfrac{\partial Az_{f_j\to s}^n}{\partial\mathbf{r}_{f_j}^n} & \dfrac{\partial El_{f_j\to s}^n}{\partial\mathbf{r}_{f_j}^n} \end{array}\right]^T \quad (24)$$

$R_{j,EO}^{f\to s}$ contains the covariance part of the father-to-son visual tracking that is not correlated with the other measurements, and is:

$$R_{j,EO}^{f\to s} = \frac{\partial\mathbf{y}_{j,EO}^{f\to s}}{\partial\boldsymbol{\rho}_{f_j}}\Sigma_{\boldsymbol{\rho}_{f_j}}^2\left(\frac{\partial\mathbf{y}_{j,EO}^{f\to s}}{\partial\boldsymbol{\rho}_{f_j}}\right)^T + \begin{bmatrix} \left(\Delta Az_{f_j\to s}^n\right)^2 & 0 \\ 0 & \left(\Delta El_{f_j\to s}^n\right)^2 \end{bmatrix} \quad (25)$$

with $\Sigma_{\boldsymbol{\rho}_{f_j}}$ diagonal matrix including father attitude uncertainty (STD), and $\dfrac{\partial\mathbf{y}_{j,EO}^{f\to s}}{\partial\boldsymbol{\rho}_{f_j}} = \begin{bmatrix} \dfrac{\partial Az_{f_j\to s}^n}{\partial\boldsymbol{\rho}_{f_j}} & \dfrac{\partial El_{f_j\to s}^n}{\partial\boldsymbol{\rho}_{f_j}} \end{bmatrix}^T$.

IV. Generalized Dilution of Precision

Generalized dilution of precision (geDOP) was first introduced in [35] to extend the concept of Dilution of Precision (DOP) [40] to the mathematical structure of the cooperative filter. The concept of Dilution of Precision (DOP) [40] is commonly adopted when analyzing accuracy in GNSS-based positioning. As demonstrated in [41], the DOP represent the Cramer-Rao lower bound on pseudorange-based positioning estimation. In general, also in integrated navigation applications based on GNSS/INS/MAG fusion, the DOP, which does not account for effects of inertial sensors, can be useful to define an upper bound for the positioning error of the navigation filter. The Dilution of Precision **D**, is in charge of finding coefficients that map the GNSS pseudorange error STD (σ_{Pr}) onto the North (σ_N), East (σ_E), and Down (σ_D), expected error STD, i.e.

$$\begin{bmatrix}\sigma_N\\ \sigma_E\\ \sigma_D\end{bmatrix} = \mathbf{D}\sigma_{Pr} = \begin{bmatrix}D_N\\ D_E\\ D_D\end{bmatrix}\sigma_{Pr} \quad (26)$$

D is generally obtained by considering the positioning part of the GNSS measurement matrix. The DOP associated to the filter reported in this paper is:

$$\mathbf{D} = \sqrt{diag\left(\left(H_{GNSS\mathbf{p}}G^{-1}\right)^T\left(R_{GNSS}\right)^{-1}H_{GNSS\mathbf{p}}G^{-1}\right)^{-1}} \quad (27)$$

where *diag* is the operator extracting the diagonal from the argument matrix and the square root operator works element-wise across the vector, whilst G converts the local frame's error ($\delta\mathbf{r}^n$) in geographic coordinate error ($\delta\mathbf{p}$). The norm of **D**, identified with D, is referred to be the Geometric dilution of precision (GDOP).

The generalized Dilution of Precision (geDOP) aims at defining a quantity which has the same role of the DOP (i.e. a vector $\breve{\mathbf{D}}$ to be used in equation (26) instead of **D**), and can account not only for GNSS measurement, but for all the measurements which concur at updating the filter's state within the correction equation, with the aim of having a more realistic estimate of the filter performance. This allow the potential of the DOP to be extended to any source of measurement, and in particular within the cooperative framework introduced in this paper. As in the case of DOP, the geDOP is useful to define an upper bound for the predicted error, summarizing positioning performance in three intuitive coefficients. In this paper the geDOP is derived with respect to the specific case of the filter

described in section III, but this approach could be applied to predict the performance of any navigation filter.

As far as the filter presented in this paper is concerned, navigation performance must be estimated by accounting for GNSS, magnetometer and cooperative measurements. Therefore, similarly to equation (27) the three components of the geDOP can be expressed as:

$$\breve{\mathbf{D}} = \begin{bmatrix} \breve{D}_N \\ \breve{D}_E \\ \breve{D}_D \end{bmatrix} = \sqrt{diag_3\left(\breve{H}^T \left(\breve{R} \right)^{-1} \sigma_{Pr}^2 \breve{H} \right)^{-1}} \tag{28}$$

where $\breve{H}$ and $\breve{R}$ are, respectively, the measurement and covariance matrix that concur to geDOP definition, defined as submatrices of H and R, and $diag_3$ is the operator that extracts the first three components of the matrix's diagonal. The norm of the geDOP, defined as $\breve{D}$, quantifies the overall navigation error and expresses son positioning error in the scale of average pseudorange uncertainty. Equation (28) uses $diag_3$ in geDOP definition, instead of $diag$. Indeed, unlike equation (27), the argument of the $diag$ function is not ensured to be a 3×3 matrix, and its dimensionality depends on how $\breve{H}$ and $\breve{R}$ are defined.

Reference [35] used only the positioning part of the matrix H to compute the geDOP, neglecting the coupling effect with son attitude that holds when son-to-father tracking is used. Indeed, son-to-father visual tracking information is used both for positioning and attitude estimation, and the attitude role is emphasized as the distance between son and father is increased. Therefore, this paper introduces an extended geDOP definition that also accounts for attitude dependency. To this aim, the matrix $\breve{H}$ includes the positioning and the attitude columns of the matrix H and is:

$$\breve{H} = \begin{bmatrix} H_{coop} \\ H_{lev} \end{bmatrix} \tag{29}$$

where:

$$H_{coop} = \begin{bmatrix} H_{GNSS\mathbf{p}} G^{-1} & 0_{m\times 3} \\ 0_{1\times 3} & H_{mag\boldsymbol{\rho}} \\ H_{1\mathbf{p}} G^{-1} & H_{1\boldsymbol{\rho}} \\ \vdots & \vdots \\ H_{J\mathbf{p}} G^{-1} & H_{J\boldsymbol{\rho}} \end{bmatrix}; H_{lev} = \begin{bmatrix} 0_{2\times 3} & \begin{matrix} 1 & 0 & 0 \\ 0 & 1 & 0 \end{matrix} \end{bmatrix} \tag{30}$$

$H_{j\mathbf{p}}$ and $H_{j\boldsymbol{\rho}}$ are the positioning and attitude part (columns) of H_j, as reported in equation (20).

From a physical point of view, the inclusion of H_{lev} within $\breve{H}$, and thus in the geDOP derivation, is based on the idea that roll and pitch angles are observable and can be estimated with bounded error also in GNSS-challenging conditions and in absence of cooperative measurements. As a consequence, since heading is also observable, the unknowns only include position components (three scalars), and assuming that the relative geometry is properly selected cooperative aiding can keep son positioning errors bounded even in the case of a single GNSS residual (M = 1) and a single father (J = 1) with son-to-father visual aiding, which provide three independent scalar measurements (one pseudorange residual and two angular residuals). This behavior has been observed in past analyses [35], [36].

From a mathematical point of view, inclusion of H_{lev} allows matrix inversion in equation (28) and thus geDOP calculation also in the above case (M = 1 and J = 1 with camera aiding), where H_{coop} is a 6×4 matrix and thus not invertible.

Besides including H_{lev} in $\breve{H}$, it is necessary to associate to roll and pitch a heuristic estimate of their uncertainty in the considered flight conditions (σ_φ and σ_θ, respectively), which are included in the covariance matrix $\breve{R}$ that concurs to geDOP definition. Therefore $\breve{R}$, can be obtained from R, defined in equation (7), as:

$$\breve{R} = \begin{bmatrix} R_{GNSS} & 0_{m\times 1} & 0_{m\times 5J} & 0_{m\times 1} & 0_{m\times 1} \\ 0_{1\times m} & R_{mag} & 0_{1\times 5J} & 0 & 0 \\ 0_{5J\times m} & 0_{5J\times 1} & R_c & 0_{5J\times 1} & 0_{5J\times 1} \\ 0_{1\times m} & 0 & 0_{1\times 5J} & \sigma_\varphi^2 & 0 \\ 0_{1\times m} & 0 & 0_{1\times 5J} & 0 & \sigma_\theta^2 \end{bmatrix} \tag{31}$$

To have a more realistic estimate of the geDOP, the positioning uncertainty of the father, included in the cooperative covariance matrix (R_c), is estimated accounting for the father dilution of precision (based on satellites seen by that platform). Finally, it is worth noting that heading uncertainty in general contributes to geDOP through R_{mag}. If magnetometer-less architectures are considered, or if heading accuracy is driven in general by other sensors (e.g., tactical grade gyros), then the resulting heading accuracy should be used in the definition of geDOP (i.e., within R_{mag}) instead of the magnetometer one.

V. Results

The performance of the proposed approach used to bound the navigation error in GNSS challenging environment, is discussed by using simulated and flight test data in sections V.C and V.D, respectively. Section V.B provides a detailed discussion about geDOP properties and analyzes the variation of this parameter as a function of the sensor(s) used for relative sensing and the number and geometry of fathers. The simulation results are obtained using the scenarios identified in section V.A, assuming the GNSS receiver can acquire GPS and GLONASS data.

A. Simulated Scenarios

This paper analyses three common scenarios that typically imply GNSS coverage issues. Specifically, inspection of a high building, flight in an urban canyon, and bridge inspection are taken into account in this work, considering real world scenarios, imported from OpenStreetMap.

Building inspection scenario, reported in Fig. 4 is relevant to a building in the Business District in Naples. Whereas, the Golden Gate bridge (San Francisco) in Fig. 5 has been considered for the bridge inspection mission. Fig. 6 depicts the urban canyon scenario, relevant to a complex of some buildings near south Cove park in lower Manhattan. The

trajectory covered by the son UAV in each scenario, is depicted in the tree figures with a blue line.

B. geDOP Analysis

Fixing the GNSS satellite geometry and the sensor specifics, the geDOP varies as a function of the relative geometry among son and father(s), and of the cooperative measurement sources selected to perform aiding. This section aims at evaluating the geDOP variation as a function of these two aspects. To this aim, an intuitive visualization has been used from Fig. 7 to Fig. 11 reporting in polar coordinates the value of the geDOP norm as a function of the relative azimuth and elevation of the father with respect to the son in NED. Constant range has been assumed. The so defined plot is called geDOP map and includes Azimuth and Elevation of the GNSS satellites in view, reported with black asterisks. For the geDOP map estimation, the son is assumed to be in the point of the trajectory where the DOP value is the highest. White areas, breaching one or both father requirements (i.e. being always in LOS with the son and having a good GNSS coverage), are forbidden to the cooperative vehicle. It is worth noting that even if white areas are forbidden to the father, they do not always identify obstructed directions. Indeed, as shown by Fig. 8.a, there could be white areas which include one or more satellites. These specific points or areas violate only one of the two requirements for placing a father, i.e., they do not ensure good GNSS coverage. Yellow areas identify values where the geDOP is higher than a threshold, that must be avoided by the cooperative vehicle to provide the son with its required positioning accuracy. The cooperative measurement sources reported in equation (2) and (3) give different contribution to positioning aiding. Indeed, due to their nature, camera measurements (Az and El) are able to provide position aiding only on the plane orthogonal to the relative line of sight between UAVs. Whereas, ranging instruments provide information along the line of sight, which makes them complementary with respect to cameras. This complementarity is also found in the geDOP maps and thus in the father-son geometries needed to effectively complement GNSS coverage in challenging environments minimizing the geDOP metric. For the sake of concreteness, figures from 7 to 11 are obtained assuming the geDOP threshold equal to 2.5, δ_R = 0.5 m and δ_{cam} = 0.07°.

With reference to the building inspection scenario, Fig. 7 reports the geDOP map with a) son-to-father, b) father-to-son, c) ranging aiding, in case a single father is used. The range is kept constant and equal to 40 m. Fig. 7.a and Fig. 7.b show a similar dependence as a function of the relative geometry, because of the similarity in the position-dependent part of the measurement matrix for father-to-son and son-to-father visual tracking. For similar (son and father) attitude uncertainties, father-to-son and son-to-father tracking exhibit a similar behavior. Whereas, in case father attitude is estimated with better accuracy (better GNSS coverage and/or higher IMU performance) the father-to-son visual tracking provides improved positioning performance, i.e. lower geDOP. Ranging aiding results offer a narrow area where the father can be placed. These geDOP values, although higher on average than the visual tracking cases, show a region without discontinuities where the father can fly. This property is essential when dealing with planning and guidance for father trajectory as in [36]. Indeed, in the case a discontinuity (yellow area) exists in the geDOP map, father could easily fall during its motion in undesired conditions spoiling the advantage of cooperation.

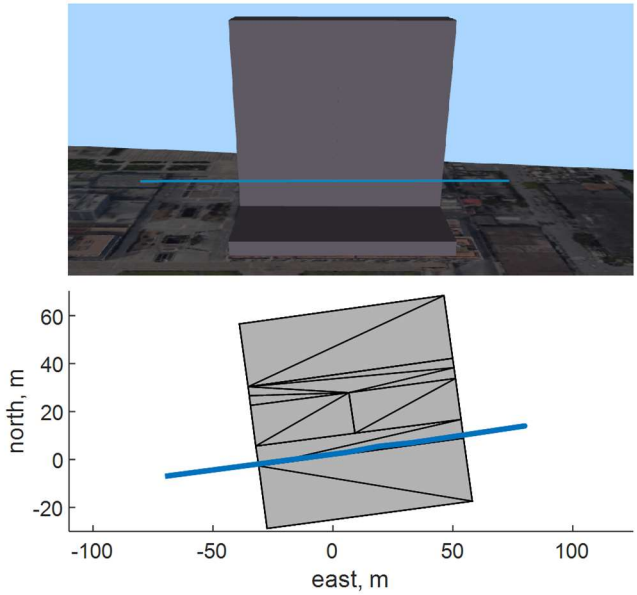

Fig. 4. Building Inspection Scenario, the son's trajectory is depicted in blue.

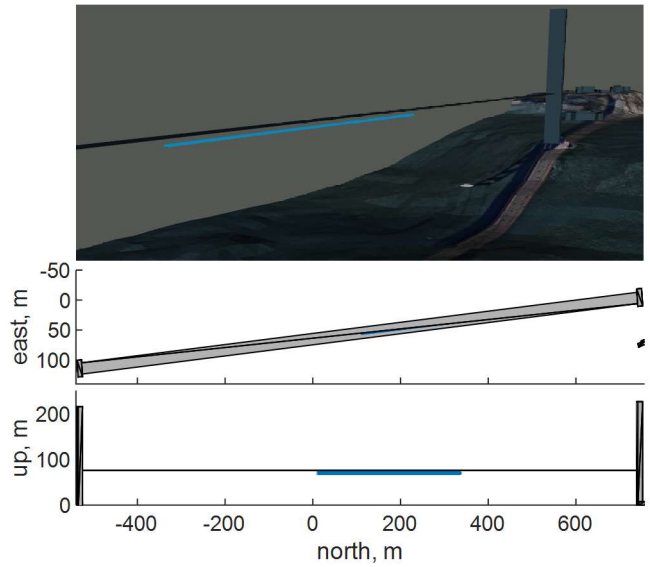

Fig. 5. Bridge Inspection Scenario, the son's trajectory is depicted in blue.

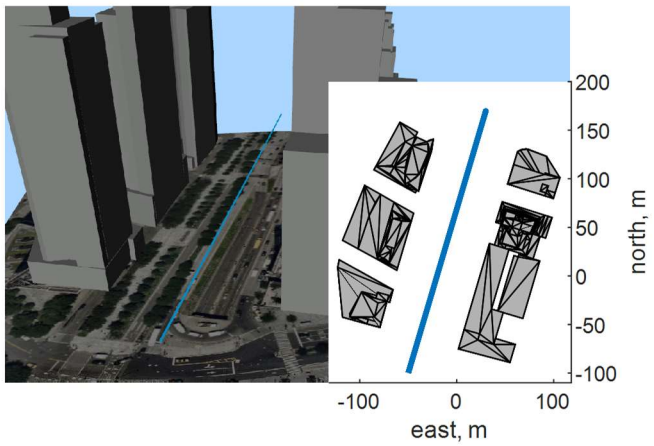

Fig. 6. Urban Canyon Scenario, the son's trajectory is depicted in blue.

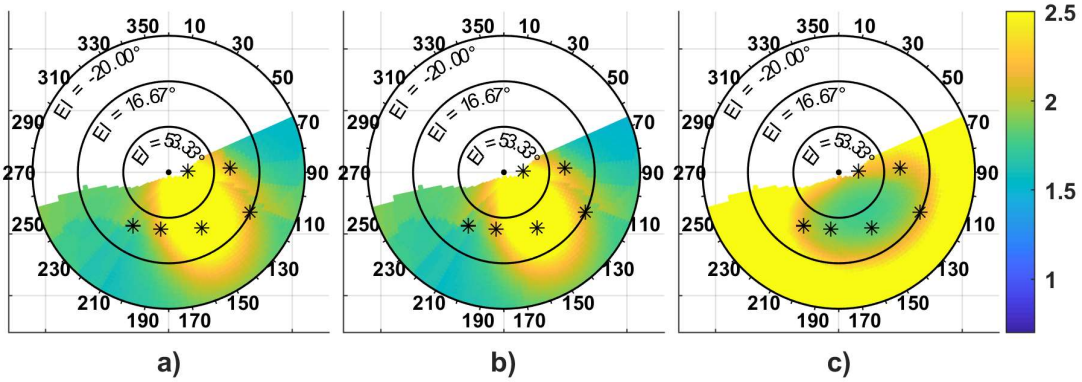

Fig. 7. geDOP norm as a function of Azimuth and Elevation in Building inspection scenario. a) son-to-father visual tracking, b) father-to-son visual tracking, c) ranging instrument. The distance of the cooperative formation has been set to 40 m.

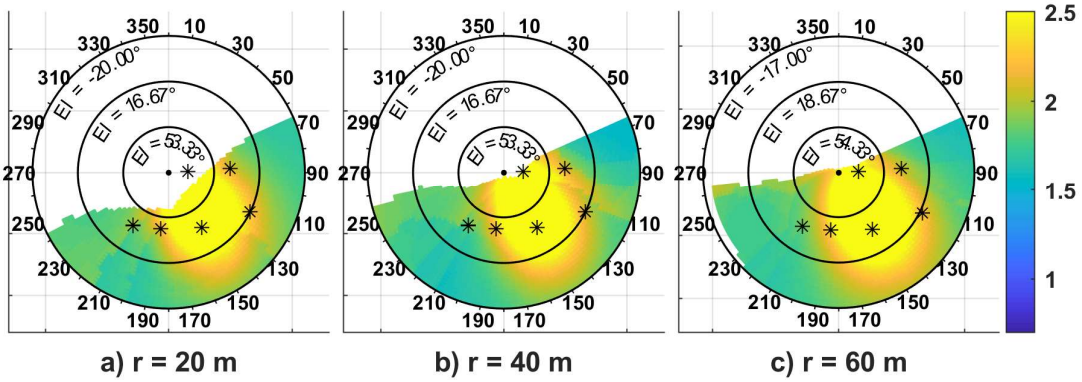

Fig. 8. geDOP norm as a function of Azimuth and Elevation in Building inspection scenario. Son-to-father aiding has been used, and range variation has been taken into account, being the range 20, 40 or 60 m respectively in a), b) and c).

The inclusion of father DOP in the geDOP estimation strengthens its dependency on the range. Fig. 8 shows the geDOP map when son-to-father camera aiding is used in the building inspection scenario by varying the distance between the two platforms. In Fig. 8.a the available positions for the father are limited due to the reduced distance between the platforms that makes the father easily fall in the challenging area. Not only does the range increase provide a larger amount of available formation geometries, but it also reduces the positioning error of the father, enabling its receiver to see more satellites. Nonetheless, when using camera, a large range is responsible of an increasing geDOP, spoiling the beneficial effect of the reduction of father positioning error. The geDOP increase with range in father-to-son tracking is due to the large camera measurement error, namely $\Delta\chi^n$ in equation (16), that linearly depends on the distance between the two platforms. This effect is stronger in son-to-father tracking, where the performance of cooperation in position aiding reduces in favor of an improved accuracy in attitude estimation (see Fig. 8).

Fig. 9 and Fig. 10 report the geDOP map when more than a father is used and refer to son-to-father visual tracking aiding and ranging aiding, respectively. The map expresses the geDOP, while the position of the first / first and second fathers is fixed and marked with red asterisks in these figures. As an example, Fig. 10.a is relevant to ranging instrument and is derived by assuming the first father is placed in the position that minimizes the norm of the geDOP in Fig. 7.c. Fig. 9 and Fig. 10 remark the camera effectiveness in cooperative navigation. Indeed, cameras allow achieving a value of the geDOP lower than the one ranging provides. In addition, ranging-based geDOP reaches a lower bound when two fathers are used, thus making a third platform useless. Whereas, in camera-based architectures the positioning error of the son keeps reducing when a new father is added.

Finally, Fig. 11 depicts the geDOP map in a) urban canyon and b) bridge inspection case. The son-to-father distance it is assumed to be 50 m and father-to-son tracking has been used. The canyon is the most complex scenario where to perform cooperation, due to the few available locations for the cooperative platform. In this specific scenario it is recommended to have an additional father, unless the father can attain very fine pointing which allows range to be increased.

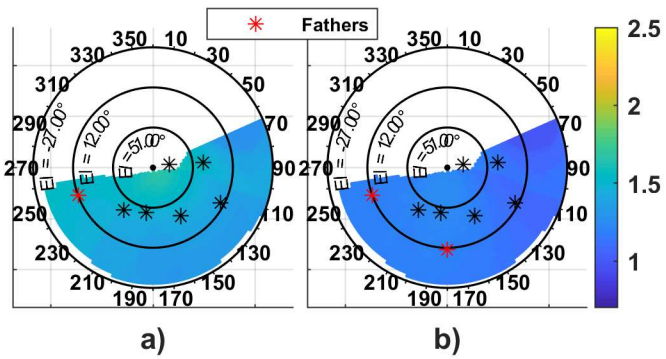

Fig. 9. geDOP norm as a function of Azimuth and Elevation with multiple fathers. Son-to-father camera aiding. a) and b) draw the geDOP maps for the second and the third father, respectively. The positions of the already fixed fathers are highlighted with red asterisks.

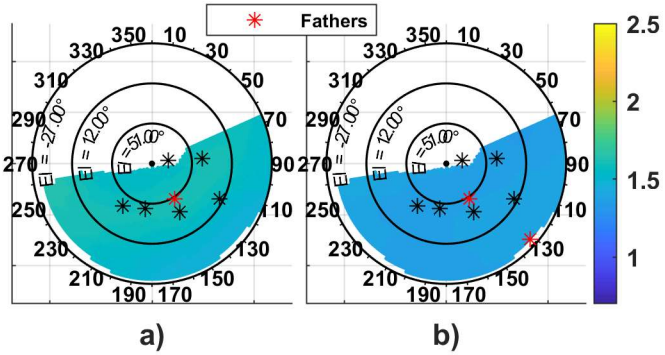

Fig. 10. geDOP norm as a function of Azimuth and Elevation with multiple fathers. RF ranging aiding. a) and b) draw the geDOP maps for the second and the third father, respectively. The positions of the already fixed fathers are highlighted with red asterisks.

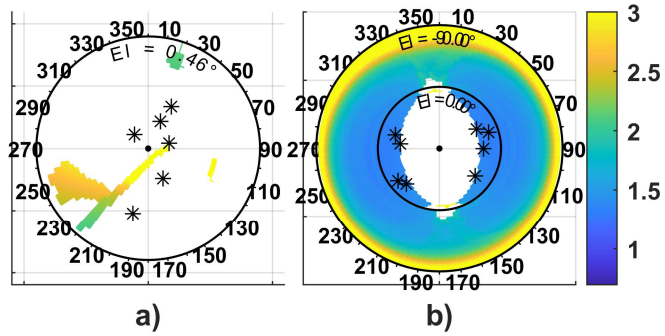

Fig. 11. geDOP map in a) urban canyon and b) bridge inspection, using father-to-son tracking. The father-to-son range it is 50 m. The norm of dilution of precision without father aiding is a) 3.86 and b) 5.34.

C. *Simulation results*

Several simulations have been carried out to assess the effectiveness of the geDOP. The performance of the navigation filter of the son with and without the father support have been compared. Son is assumed to embark a consumer grade IMU, whose parameter are reported in Table I. In each simulation, the father(s) is flying along a trajectory parallel to the son, with a separation defined with the aim to minimize the geDOP.

TABLE I
SIMULATED IMU PARAMETERS

Velocity RW, [m/s/√h]	Acc. bias stability, [mg]	Acc. bias repetab. [mg]	Angular RW [°/√h]	Gyro bias stability [°/h]	Gyro bias repetab. [°/h]
0.06	0.11	8	0.6	38	500

RW is the Random Walk

Fig. 12 shows the accuracy of son positioning that is achieved using a cooperative father within the bridge inspection framework. Father-to-son camera aiding has been used. Therefore, Fig. 11.b has been used as reference to select the best position for the father when supporting the son flight. It is worth noting that geDOP maps are obtained for a specific position of the son along its trajectory, that corresponds to the worst coverage condition, i.e. maximum DOP. In general, the value of geDOP estimated for each time instant is not constant and varies as a function of the father positioning error and the GNSS satellites seen by the son vehicle.

The errors on the NED position components ($\mathbf{r}_s$(N), $\mathbf{r}_s$(E) and $\mathbf{r}_s$(D), respectively) obtained with the cooperative aiding of a single father are shown in black in Fig. 12, whereas the filter outcome without cooperation, i.e. no father support, is shown in gray. Without cooperation, the filter results represent the solution that could be achieved only accounting for GNSS, IMU and magnetometer measurements. Background color shows the norm of the DOP the son encounters along its trajectory, i.e. the GDOP, which is a performance index of the INS/GNSS/MAG filter, as anticipated in section IV. Root mean square (RMS) and maximum errors are reported for each component, both for the solution with and without cooperation, in black and gray respectively. Equation (26) has been used to estimate the value of the error STD of the three NED components (σ_N, σ_E, σ_D), using either the DOP values (equation (27)) or the geDOP value (equation (28)). The mean value obtained along the trajectory is reported either in gray (for the DOP) or in black (for the geDOP). σ_N, σ_E and σ_D estimated using the geDOP (with equations (26) and (28)) have been used to plot the 3σ bound, defined by the transparent shape.

As shown by the figure, the 3σ bound predicted using the geDOP actually contains filter errors, and looks a little over conservative for the vertical component. As anticipated in section IV, this comes from ignoring inertial propagation when predicting DOP and geDOP, that allows them only to provide an estimate for the filter performance lower bound (i.e. error upper bound). Nevertheless, for all components, it can be seen that the ratio between RMS errors with and without cooperation is similar to the ratio between geDOP and DOP components, thus proving the geDOP effectiveness in predicting the improvement in positioning.

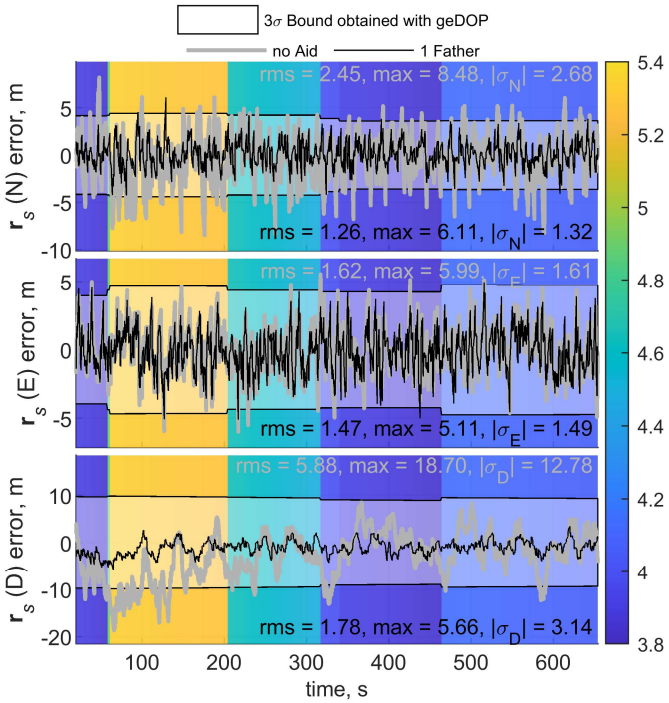

Fig. 12. Son's navigation results, bridge inspection scenario. NED positions' errors. Father-to-son camera aiding. Relative formation has been chosen in order to optimize the cooperative aiding (minimizing the geDOP norm): Az = 90°, El = 6°, r = 40 m. Background color represents the value of the GDOP of the GNSS constellation along the trajectory. 3σ bound of the expected filter performance has been estimated predicting the geDOP along the trajectory.

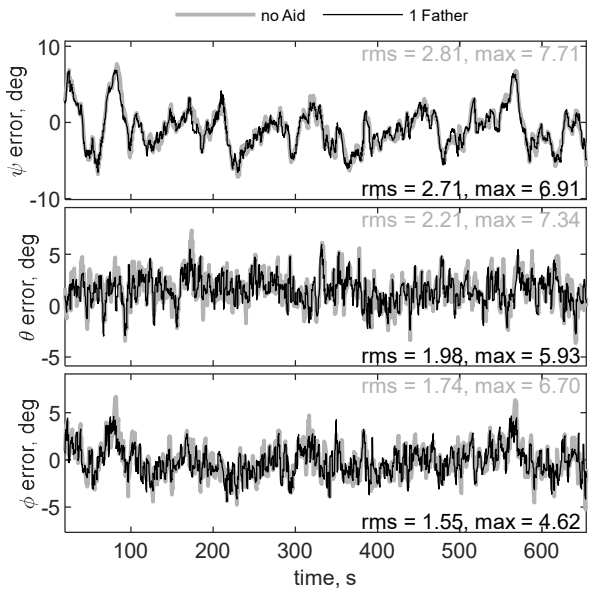

Fig. 13. Son's navigation results, bridge inspection scenario. Heading (ψ), pitch (θ) and roll (ϕ) errors. Father-to-son camera aiding. Relative formation: Az = 90°, El = 6°, r = 40 m.

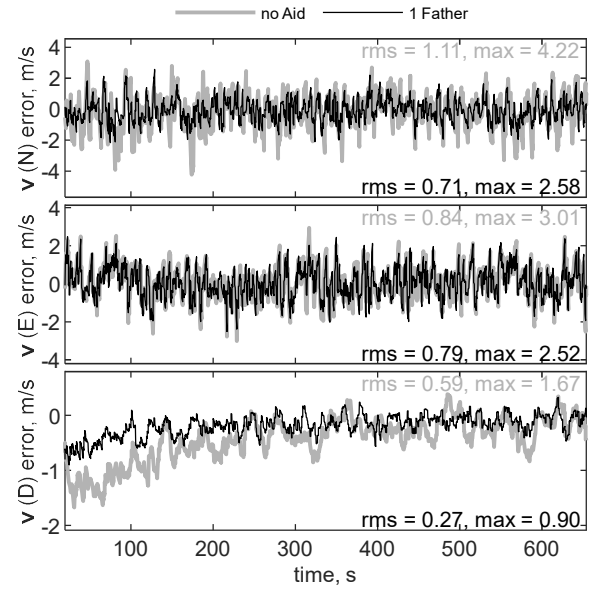

Fig. 14. Son's navigation results, bridge inspection scenario. NED velocity errors. Father-to-son camera aiding. Relative formation: Az = 90°, El = 6°, r = 40 m.

The same information is reported in Table II, which includes quantitative estimates of these ratios. The father-to-son formation used in Fig. 12 assumes their separation is mostly in the East direction. Therefore, when camera aiding is used, the East component of the son's position is almost unobservable and therefore takes the least advantage from cooperation, as shown in line 2 of Table II. For the sake of completeness, the angles and velocity results provided by the filter are reported in Fig. 13 and Fig. 14. Single vehicle based solutions (no father) are reported with the gray line.

To further highlight the consistency between the geDOP metric and the navigation accuracy, within the same scenario relevant to Fig. 12, a different father trajectory has been simulated with relative azimuth and elevation that reduce the cooperation effectiveness, maximizing, instead of minimizing, the geDOP norm in Fig. 11.b. Therefore, a relative geometry with Az = 90° and El = -80° has been assumed. Fig. 15 shows the NED positioning errors given by the cooperative filter using father-to-son camera aiding and filter's performance indicators (RMS and DOP/geDOP-based STD), as in Fig. 12, but assuming the above reported formation geometry. As expected, the predicted 3σ bound based on geDOP prediction increases, especially in the Down component that is almost parallel to the relative distance, thus retrieving low benefit from cooperation if camera aiding is used.

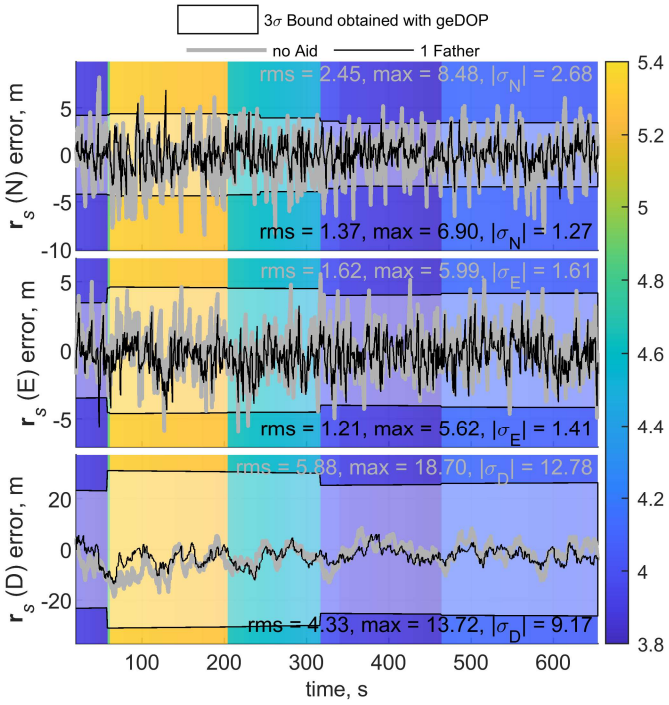

Fig. 15. Son's navigation results, bridge inspection scenario. NED positioning errors. Father-to-son camera aiding. Relative formation has been chosen in order to penalize cooperative aiding (maximizing geDOP norm): Az = 90°, El = -80°, r = 40 m. Background color represents the value of the GDOP of the GNSS constellation along the trajectory. 3σ bound of the expected filter performance has been estimated predicting the geDOP along the trajectory.

TABLE II
COMPARISON OF RMS ERRORS AND GEDOP-BASED STD WITH COOPERATION (1 FATHER Az = 90°, El = 6°, r = 40 m) AND WITHOUT COOPERATION, BRIDGE INSPECTION SCENARIO

Component		Filter resulting RMS [m]		Predicted STD ($\lvert\sigma_h\rvert$) [m]	
		Value	Ratio (coop/uncoop)	Value	Ratio (coop/uncoop)
$\mathbf{r}_s$(N)	Without Cooperation	2.45	0.60	2.68	0.50
	With Cooperation	1.26		1.32	
$\mathbf{r}_s$(E)	Without Cooperation	1.62	0.91	1.61	0.93
	With Cooperation	1.47		1.49	
$\mathbf{r}_s$(D)	Without Cooperation	5.88	0.30	12.87	0.25
	With Cooperation	1.78		3.14	

geDOP is effective in predicting filter performance, and the increase in the computed RMS errors is consistent with the geDOP variation.

When son-to-father camera aiding is used, as shown in Fig. 16 cooperative navigation performance can be spoiled by the son attitude uncertainty. However, a better IMU mounted on the son could improve the cooperative formation performance, as highlighted in red in Fig. 16. Specifically the figure reports in the bridge inspection case the position error of the navigation filter in the case no aiding (gray) and 1 father (black or red line) is used. Son-to-father camera is used, and the son is assumed to embark either the IMU whose specifics are reported in Table I (black line) or an IMU with better performance reported in the figure as "high grade IMU" (red line). The latter is assumed to have the same accelerometers but much better gyroscopes (e.g. bias stability 0.25°/h vs 38°/h) than the lower grade ones reported in Table I. RMS error and maximum error for the uncooperative and cooperative solution are reported in the figure along the mean of the DOP/geDOP-based STD, predicted with equations (26) and (28).

Cooperative navigation performance as a function of the father positioning and attitude errors is reported in Table III, when camera is used. RMS and maximum error are used as reference parameters. The STD error on father position is obtained by multiplying the user equivalent range error (UERE) by the current father's DOP to obtain the error on each component. Result of Table III are obtained in the bridge inspection scenario with relative azimuth and elevation respectively equal to 90 and 6 deg. The distance between father and son is 40 m.

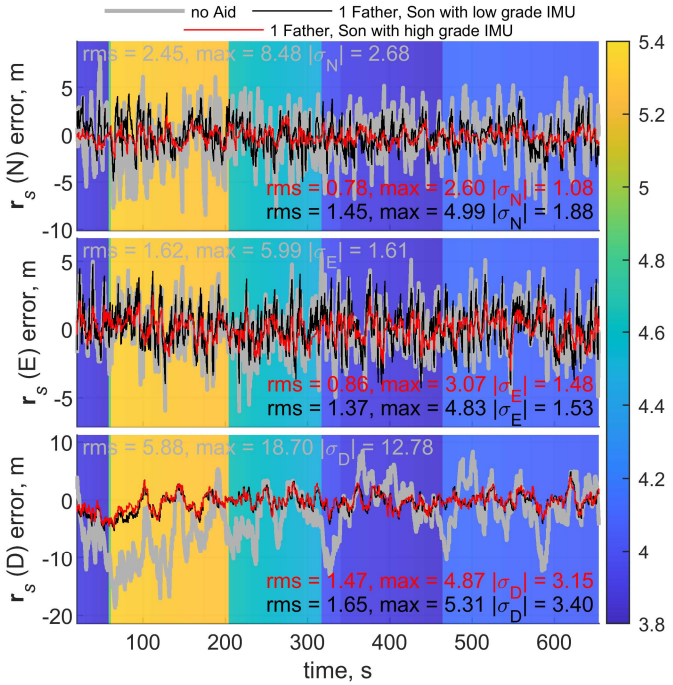

Fig. 16. Son's navigation results, bridge inspection scenario. NED positioning errors. Son-to-Father camera aiding. Relative formation has been chosen in order to optimize the cooperative aiding (minimizing the geDOP norm): Az = 90°, El = 6°, r = 40 m. Black and red lines represent camera aiding with two different IMUs mounted on the son: low and high grade respectively. Low grade IMU parameters are reported in Table I, whereas the high grade IMU has been assumed to have the same accelerometers' parameters reported in Table I, but much better gyroscopes (e.g. bias stability 0.25°/h vs 38°/h). Background color represents the value of the GDOP the son encounters.

TABLE III
COOPERATIVE NAVIGATION PERFORMANCE AS A FUNCTION OF FATHER'S NAVIGATION ERRORS: CAMERA AIDING.

Father Error		**Cooperative Aiding**	**Son positioning performance**, m $[x_N, x_E, x_D]$
Attitude STD, deg $[\phi, \theta, \psi]$[a]	Position STD, m		
[0.5,0.5,1]	3	Father-to-son	RMS = [1.26, 1.47, 1.78] Max = [6.11, 5.11, 5.66]
		Son-to-father	RMS = [1.45, 1.37, 1.65] Max = [4.99, 4.83, 5.31]
		Father-to-son + RF ranging	RMS = [1.26, 1.05, 1.84] Max = [6.12, 3.81, 5.69]
[1,1,3]	3	Father-to-son	RMS = [1.44, 1.47, 1.86] Max = [5.39, 5.32, 5.96]
		Son-to-father	RMS = [1.45, 1.37, 1.65] Max = [4.99, 4.83, 5.31]
[0.5,0.5,1]	0.3	Father-to-son	RMS = [0.44, 1.46, 0.39] Max = [1.58, 5.24, 1.20]
		Son-to-father	RMS = [1.04, 1.29, 0.77] Max = [4.14, 4.66, 2.67]

Results refer to bridge inspection scenario. Relative formation: Az = 90°, El = 6°, r = 40 m, and low grade IMU (Table I) on the son.
[a] ϕ, θ, ψ are roll pitch and heading angles, respectively.

A better father's attitude accuracy only affects the father-to-son tracking scenario. Whilst, both the camera tracking strategies benefit from an improvement in father position accuracy. Therefore, differential or carrier phase differential GPS brings a huge advantage to the cooperative navigation strategy even if only used on the cooperative platform. However, Table III shows that the east component's error remains almost unaltered from father's accuracy variation because it is unobservable with the assumed geometry if a camera is used. On the other hand, complementing camera with ranging would reduce the error on that component. Indeed, ranging acts in the direction parallel to the UAVs separation.

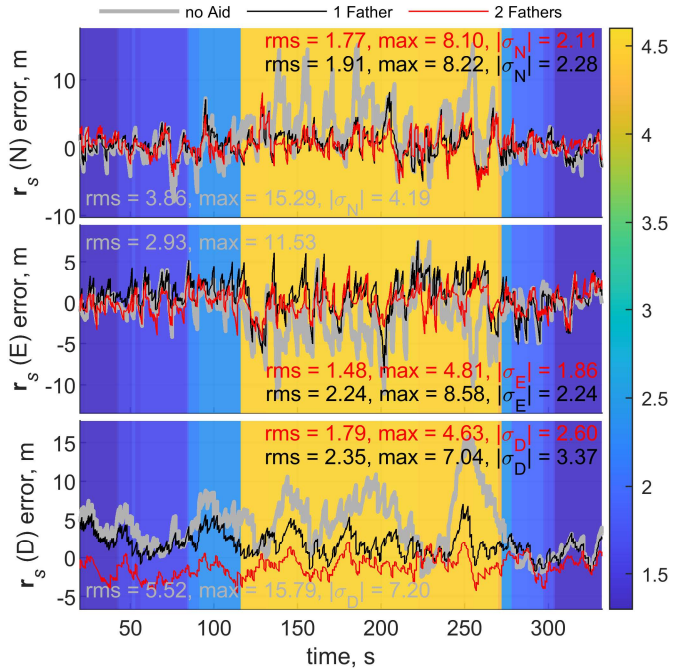

Fig. 17. Son's navigation results, building inspection scenario. NED positions' errors. Son-to-Father camera aiding with one or two fathers. Father 1: Az = -110°, El = 12°, r = 40 m. Father 2: Az = 180°, El = 10°, r = 30 m. Background color represents the value of the GDOP of the son.

Finally, Fig. 17 shows the filter results in a building inspection scenario, by sequentially adding fathers. The figure highlights the advantage in using a second father. Son-to-Father camera aiding is used and the best position for the two fathers must be defined by using Fig. 9. Specifically, the two fathers are placed in the position highlighted by the red asterisks in Fig. 9.b. The figure reports the positioning error of the son by using one (black) or two (red) additional fathers along with the results obtained without cooperation (gray). RMS and Maximum error of the filter results and time average of the error STD on the three NED components predicted using the geDOP and DOP have been reported.

D. Experimental Setup and Results

The effectiveness of the proposed strategy in guaranteeing a bounded positioning error when flying under non nominal GNSS coverage, is demonstrated in this section using experimental data. An image from the executed flight tests is reported in Fig. 18. Multi-constellation (GPS and Galileo) data have been taken into account. The experimental setup used in this framework includes two customized DJI™ M100 platforms equipped with an additional GNSS single frequency receiver (uBlox™ LEA-M8T) with raw measurements capabilities:

- The "son" is equipped with an onboard computer (Intel NUC™ with an i7 CPU) and a CCD camera (PointGrey Flea™ FL3-U3-20E4C-C with 1600 X 1200 resolution in pixels and maximum frame rate of 59 fps, equipped with 8 mm focal length optics, with a resulting IFOV of about 0.030°).
- The "father" embarks as onboard computer an Intel NUC™ with i5 CPU and a CCD camera (PointGrey BlackflyTM BFLY-U3-50H5C-C with 2448 X 2048 resolution in pixels and maximum frame rate of 7.5 fps, equipped with 6 mm focal length optics, with a resulting IFOV of about 0.022°).

Fig. 19 shows the customized setup on board one of the M100, i.e. the son UAV. The additional GNSS antenna has been mounted symmetrically to the native one. Both the GNSS antennas have been mounted on a carbon fiber rod higher than the DJI default to prevent magnetic interference that could arise in proximity of the on-board computer. Onboard computer power supply is provided by the M100 battery via a DC-DC adapter as suggested in [42].

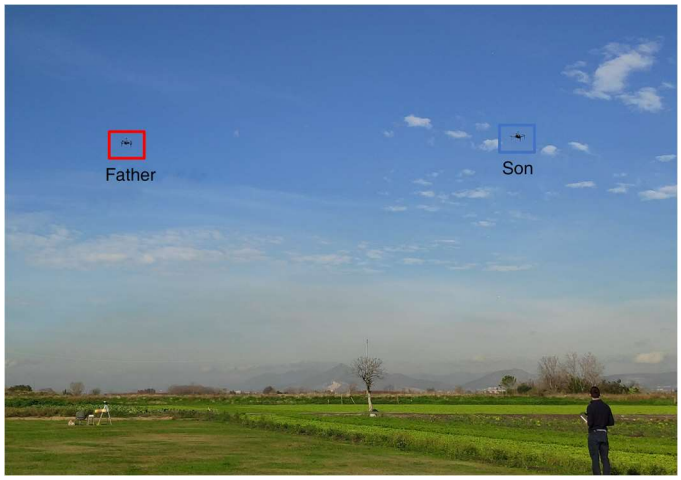

Fig. 18. Flight test Image taken from ground

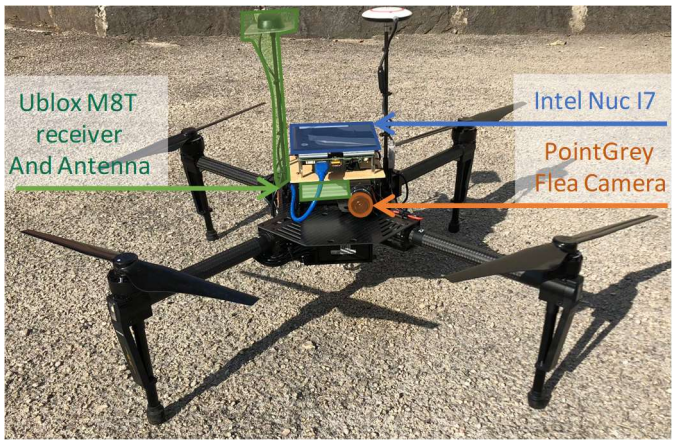

Fig. 19. Costumized setup on-board the son UAV.

Data acquisition software has been developed in ROS (Robot Operating System), writing a customized ROS node able to process online the GNSS measurement and get an accurate time tag. Accurate satellites' position along with the corrected pseudoranges from ionospheric and tropospheric error has been retrieved offline thanks to a customized version of the RTKLIB software [43] using broadcast ephemeris. As concerns image processing for visual detection and tracking, the authors developed ad hoc algorithms that exploit the cooperative nature of these applications, and their most recent works include deep learning approaches [44], with very promising results. In the experiment described in this paper, these approaches were complemented with a supervised procedure, being the focus set on the cooperative navigation algorithm. Camera-IMU calibration, aimed at identifying the fixed rotation matrix between the IMU (body) and Camera frame in a strapdown installation, and IMU parameter estimation have been performed with the Kalibr open source software [45]. The so estimated IMU parameters are reported in Table IV for the son UAV.

The flight test has been performed outdoor under nominal GNSS conditions, allowing an accurate estimate of the drone position through the onboard navigation filter, to be used as benchmark. Then, GNSS-challenging conditions have been simulated offline by assuming a virtual 3D environment and removing the satellites whose ray-path would intersect the surrounding obstacles. Specifically, a bridge inspection scenario, depicted in Fig. 20, has been used. Fig. 20 shows the trajectories of the two vehicles (son and father) in the 3D environment, composed by a virtual bridge, located above the trajectory of the son. Adding the virtual obstacle yields a trajectory for the son that is always in challenging conditions, as remarked by the GDOP with removed satellites, reported in Fig. 20.b with the colored dots. It shows very bad coverage which would impact the navigation performance of a standard GNSS-IMU navigation filter.

TABLE VI
IMU PARAMETERS ESTIMATED WITH KALIBR [45]

Velocity RW, [m/s/√h]	Acc. bias stability, [mg]	Angular RW [°/√h]	Gyro bias stability [°/h]
0.53	0.48	0.37	11.06

RW is the Random Walk

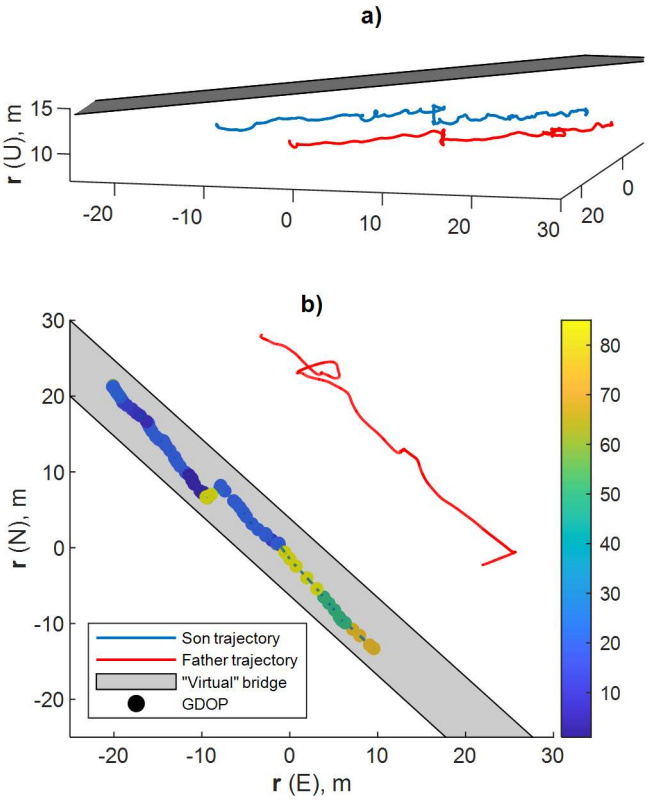

Fig. 20. Trajectory of the two UAVs and simulated bridge. The colored dots represent the GDOP of the son with removed satellites due to the obstacle.

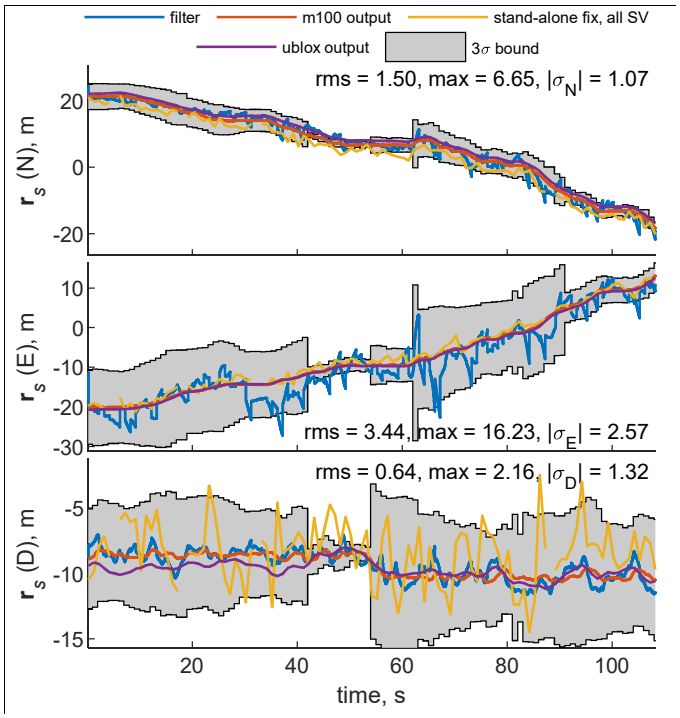

Fig. 21. Results of the cooperative navigation algorithm using son-to-father visual tracking on experimental data. Galileo and GPS satellites are used. The gray background defines the 3σ bound interval, estimated with eqs. (26) and (28).

Conversely, using cooperation bounds the positioning errors along the whole flight as shown in Fig. 21, which reports North-East-Down position components as estimated by the EKF described in this paper and supported by son-to-father visual aiding. This solution is defined as "filter" within the figure legend, and it is depicted in blue. The figure also includes other positioning solutions, as follows:

- the solution of the onboard autopilot navigation filter, operating in open sky conditions, defined as “M100 output”, in red. This solution can be assumed as a (metric level) reference;
- the solution of the onboard uBlox M8T^{TM} receiver, operating in open sky conditions, defined as “ublox output”, in purple;
- the position solution calculated on the basis of all the raw pseudorange measurements gathered by the uBlox receiver, in open sky conditions (no virtual obstacles are considered). This is defined as “standalone fix, all SV” and depicted in yellow.

The positioning solution for the EKF assuming the simulated bridge and no cooperation is not reported, since the very large errors would impact the scale of the diagrams.

As in the numerical simulations, 3σ bounds estimated with geDOP and equations (26) and (28) have been included in Fig. 21 as gray background. Filter estimates always lie within the 3σ bounds with the exception of a very few instants, pointing out that geDOP can be used to predict upper bounds for the expected positioning error. Those rare events are related to anomalous pseudoranges and/or sudden maneuvers of the son. The value of the geDOP is higher in the East component than in the North, because the relative position vector between the platforms is almost parallel to the East direction, and camera aiding is not effective along that direction, as anticipated in section V.B. Finally, the usage of cooperative measurements allows considerably reducing the vertical error, even if compared with the performance of the stand-alone GNSS fix obtained under nominal coverage.

Fig. 21 reports the RMS and maximum errors experienced by the filter, evaluated assuming as reference the position estimates of the onboard autopilot navigation filter (“M100 output”). The time average of the geDOP-based error standard deviations estimated along the trajectory has also been reported. A good consistency is observed for North and East errors, while for the vertical component the RMS error is below $|\sigma_D|$. These results can be explained considering as in the numerical cases the role of propagation and of inertial sensors, but also the metric-level uncertainty of the positioning estimates assumed as reference (M100 output exploits standalone GNSS measurements).

VI. Conclusion

This paper discussed an approach to improve navigation performance for UAVs flying in GNSS-challenging conditions, which is based on cooperative aircraft flying in open sky conditions and thus under reliable satellite coverage. To this aim, a tightly coupled EKF exploiting cooperative measurements and partial GNSS information was developed. The filter was tested on simulated and experimental data using multi-constellation GNSS, demonstrating the capability to

provide bounded positioning error in very high DOP conditions, and even in absence of GNSS position fix.

The concept of generalized dilution of precision was introduced as a powerful tool to predict positioning performance, demonstrating satisfying consistency with filter performance both in simulations and in flight tests. While it derives from the idea of extending the DOP concept to cooperative navigation measurements, it not only depends on geometric parameters (both regarding GNSS satellites in view and configuration of cooperative UAVs), but actually includes technology-dependant effects, such as the performance of the sensors (e.g., vision, RF ranging, inertial) embarked on son and father UAVs. Thus, geDOP provides a flexible and sensor agnostic tool to predict navigation performance, either in real time or off-line, which can account for all information sources linked to vehicle positioning. Indeed, geDOP applicability is not restricted to GNSS challenging environments, as the concept is applicable to all the scenarios where positioning accuracy can be improved through multi-vehicle cooperation. As it happens for the DOP, the geDOP can give a quantitative information about the actual positioning error experimented by the filter only regarding the correction equation, since it does not account for the prediction phase of the navigation algorithm. Further developments aim at defining a geDOP-inspired indicator which can accurately predict filtering error, also accounting for propagation model.

Current research is also aimed at implementing the cooperative navigation concept described in this paper in real world mission scenarios, such as mapping and inspection in GNSS-challenging environments.

REFERENCES

[1] M. Mozaffari, W. Saad, M. Bennis, Y. Nam, and M. Debbah, "A Tutorial on UAVs for Wireless Networks: Applications, Challenges, and Open Problems," *IEEE Commun. Surv. Tutorials*, p. 1, 2019, doi: 10.1109/COMST.2019.2902862.

[2] I. Miller, B. Schimpf, M. Campbell, and J. Leyssens, "Tightly-coupled GPS / INS system design for autonomous urban navigation," in *2008 IEEE/ION Position, Location and Navigation Symposium*, 2008, pp. 1297–1310, doi: 10.1109/PLANS.2008.4570084.

[3] N. Zhu, J. Marais, D. Bétaille, and M. Berbineau, "GNSS Position Integrity in Urban Environments: A Review of Literature," *IEEE Trans. Intell. Transp. Syst.*, vol. 19, no. 9, pp. 2762–2778, 2018, doi: 10.1109/TITS.2017.2766768.

[4] L. Wang, P. D. Groves, and M. K. Ziebart, "Multi-Constellation GNSS Performance Evaluation for Urban Canyons Using Large Virtual Reality City Models," *J. Navig.*, vol. 65, no. 3, pp. 459–476, 2012, doi: DOI: 10.1017/S0373463312000082.

[5] Y. Watanabe, A. Veillard, and C. Chanel, "Navigation and Guidance Strategy Planning for UAV Urban Operation," in *AIAA Infotech @ Aerospace*, American Institute of Aeronautics and Astronautics, 2016.

[6] F. De Vivo, M. Battipede, and P. Gili, "Nonvisible satellite estimation algorithm for improved uav navigation in mountainous regions," *IEEE Aerosp. Electron. Syst. Mag.*, vol. 33, no. 11, pp. 4–19, 2018, doi: 10.1109/MAES.2018.170220.

[7] P. Chattopadhyay, D. K. Jha, S. Sarkar, and A. Ray, "Path planning in GPS-denied environments: A collective intelligence approach," in *2015 American Control Conference (ACC)*, 2015, pp. 3082–3087, doi: 10.1109/ACC.2015.7171806.

[8] S. D. Bopardikar, B. Englot, and A. Speranzon, "Multi-objective path planning in GPS denied environments under localization constraints," in *2014 American Control Conference*, 2014, pp. 1872–1879, doi: 10.1109/ACC.2014.6858731.

[9] M. Obst, S. Bauer, P. Reisdorf, and G. Wanielik, "Multipath detection with 3D digital maps for robust multi-constellation GNSS/INS vehicle localization in urban areas," in *2012 IEEE Intelligent Vehicles Symposium*, 2012, pp. 184–190, doi: 10.1109/IVS.2012.6232285.

[10] K.-W. Chiang, T. T. Duong, and J.-K. Liao, "The Performance Analysis of a Real-Time Integrated INS/GPS Vehicle Navigation System with Abnormal GPS Measurement Elimination," *Sensors* , vol. 13, no. 8. 2013, doi: 10.3390/s130810599.

[11] H. Ko, B. Kim, and S. Kong, "GNSS Multipath-Resistant Cooperative Navigation in Urban Vehicular Networks," *IEEE Trans. Veh. Technol.*, vol. 64, no. 12, pp. 5450–5463, 2015, doi: 10.1109/TVT.2015.2481509.

[12] N. Kbayer and M. Sahmoudi, "Performances Analysis of GNSS NLOS Bias Correction in Urban Environment Using a Three-Dimensional City Model and GNSS Simulator," *IEEE Trans. Aerosp. Electron. Syst.*, vol. 54, no. 4, pp. 1799–1814, 2018, doi: 10.1109/TAES.2018.2801658.

[13] S. Daneshmand, A. Broumandan, N. Sokhandan, and G. Lachapelle, "GNSS Multipath Mitigation with a Moving Antenna Array," *IEEE Trans. Aerosp. Electron. Syst.*, vol. 49, no. 1, pp. 693–698, 2013, doi: 10.1109/TAES.2013.6404136.

[14] T. Ren and M. G. Petovello, "A Stand-Alone Approach for High-Sensitivity GNSS Receivers in Signal-Challenged Environment," *IEEE Trans. Aerosp. Electron. Syst.*, vol. 53, no. 5, pp. 2438–2448, 2017, doi: 10.1109/TAES.2017.2699539.

[15] S. Godha and M. E. Cannon, "GPS/MEMS INS integrated system for navigation in urban areas," *GPS Solut.*, vol. 11, no. 3, pp. 193–203, 2007, doi: 10.1007/s10291-006-0050-8.

[16] G. Chowdhary, E. N. Johnson, D. Magree, A. Wu, and A. Shein, "GPS-denied Indoor and Outdoor Monocular Vision Aided Navigation and Control of Unmanned Aircraft," *J. F. Robot.*, vol. 30, no. 3, pp. 415–438, 2013, doi: 10.1002/rob.21454.

[17] R. Madison, G. Andrews, P. A. Debitetto, S. Rasmussen, and M. Bottkol, *Vision-Aided Navigation for Small UAVs in GPS-Challenged Environments*. 2007.

[18] S. Ahrens, D. Levine, G. Andrews, and J. P. How, "Vision-based guidance and control of a hovering vehicle in unknown, GPS-denied environments," in *2009 IEEE International Conference on Robotics and Automation*, 2009, pp. 2643–2648, doi: 10.1109/ROBOT.2009.5152680.

[19] S. Weiss, D. Scaramuzza, and R. Siegwart, "Monocular-SLAM–based navigation for autonomous micro helicopters in GPS-denied environments," *J. F. Robot.*, vol. 28, no. 6, pp. 854–874, Nov. 2011, doi: 10.1002/rob.20412.

[20] K. Celik, S.-J. Chung, and A. Somani, "MVCSLAM: Mono-Vision Corner SLAM for Autonomous Micro-Helicopters in GPS Denied Environments," in *AIAA Guidance, Navigation and Control Conference and Exhibit*, American Institute of Aeronautics and Astronautics, 2008.

[21] A. Bachrach, A. de Winter, R. He, G. Hemann, S. Prentice, and N. Roy, "RANGE - robust autonomous navigation in GPS-denied environments," in *2010 IEEE International Conference on Robotics and Automation*, 2010, pp. 1096–1097, doi: 10.1109/ROBOT.2010.5509990.

[22] K. M. Pesyna Jr., Z. M. Kassas, J. A. Bhatti, and T. E. Humphreys, "Tightly-coupled opportunistic navigation for deep urban and indoor positioning," in *24th International Technical Meeting of the Satellite Division of the Institute of Navigation 2011, ION GNSS 2011*, 2011, vol. 5, pp. 3605–3616.

[23] J. J. Morales, P. F. Roysdon, and Z. M. Kassas, "Signals of opportunity aided inertial navigation," in *29th International Technical Meeting of the Satellite Division of the Institute of Navigation, ION GNSS 2016*, 2016, doi: 10.33012/2016.14652.

[24] R. Kapoor, S. Ramasamy, A. Gardi, C. Bieber, L. Silverberg, and R. Sabatini, "A Novel 3D Multilateration Sensor Using Distributed Ultrasonic Beacons for Indoor Navigation," *Sensors* , vol. 16, no. 10. 2016, doi: 10.3390/s16101637.

[25] K. Sundar, S. Misra, S. Rathinam, and R. Sharma, "Routing unmanned vehicles in GPS-denied environments," in *2017 International Conference on Unmanned Aircraft Systems (ICUAS)*, 2017, pp. 62–71, doi: 10.1109/ICUAS.2017.7991488.

[26] S. Hening, C. A. Ippolito, K. S. Krishnakumar, V. Stepanyan, and M. Teodorescu, "3D LiDAR SLAM Integration with GPS/INS for UAVs in Urban GPS-Degraded Environments," in *AIAA Information Systems-AIAA Infotech @ Aerospace*, American Institute of Aeronautics and Astronautics, 2017.

[27] Z. Zhu, S. Roumeliotis, J. Hesch, H. Park, and D. Venable, "Architecture for asymmetric collaborative navigation," in *IEEE PLANS*, 2012, pp. 777–782, doi: 10.1109/PLANS.2012.6236955.

[28] H. Mokhtarzadeh and D. Gebre-Egziabher, "Performance of networked dead reckoning navigation system," *IEEE Trans. Aerosp. Electron.*

Syst., vol. 52, no. 5, pp. 2539–2553, 2016, doi: 10.1109/TAES.2016.150180.

[29] A. J. Rutkowski, J. E. Barnes, and A. T. Smith, "Path planning for optimal cooperative navigation," in *Proceedings of the IEEE/ION Position, Location and Navigation Symposium, PLANS 2016*, 2016, pp. 359–365, doi: 10.1109/PLANS.2016.7479721.

[30] E. Cledat and D. A. Cucci, "Mapping GNSS restricted environment with a drone tandem and indirect position control," in *ISPRS*, 2017.

[31] V. Indelman, P. Gurfil, E. Rivlin, and H. Rotstein, "Real-Time Vision-Aided Localization and Navigation Based on Three-View Geometry," *IEEE Trans. Aerosp. Electron. Syst.*, vol. 48, no. 3, pp. 2239–2259, 2012, doi: 10.1109/TAES.2012.6237590.

[32] V. O. Sivaneri and J. N. Gross, "UGV-to-UAV cooperative ranging for robust navigation in GNSS-challenged environments," *Aerosp. Sci. Technol.*, vol. 71, pp. 245–255, 2017, doi: 10.1016/j.ast.2017.09.024.

[33] V. O. Sivaneri and J. N. Gross, "Flight-testing of a cooperative UGV-to-UAV strategy for improved positioning in challenging GNSS environments," *Aerosp. Sci. Technol.*, vol. 82–83, pp. 575–582, 2018, doi: https://doi.org/10.1016/j.ast.2018.09.035.

[34] A. R. Vetrella, G. Fasano, and D. Accardo, "Cooperative navigation in GPS-challenging environments exploiting position broadcast and vision-based tracking," in *2016 International Conference on Unmanned Aircraft Systems, ICUAS 2016*, 2016, pp. 447–456, doi: 10.1109/ICUAS.2016.7502647.

[35] F. Causa, A. R. Vetrella, G. Fasano, and D. Accardo, "Multi-UAV Formation Geometries for Cooperative Navigation in GNSS-challenging Environments," in *IEEE/ION PLANS*, 2018, pp. 775–785.

[36] F. Causa, M. Popović, G. Fasano, M. Grassi, J. Nieto, and R. Siegwart, "Navigation aware planning for tandem UAV missions in GNSS challenging Environments," *2019 AIAA Guidance, Navigation, and Control Conference*, 2019.

[37] T. L. Molloy, J. J. Ford, and L. Mejias, "Looming aircraft threats: Shape-based passive ranging of aircraft from monocular vision," in *Australasian Conference on Robotics and Automation, ACRA*, 2014.

[38] J. Farrell, *Aided Navigation: GPS with High Rate Sensors*, 1st ed. New York, NY, USA: McGraw-Hill, Inc., 2008.

[39] A. Caporali and L. Nicolini, "Interoperability of the GNSS's for Positioning and Timing BT - New Advanced GNSS and 3D Spatial Techniques," 2018, pp. 73–85.

[40] R. B. Langley, "Dilution of precision," *GPS world*, vol. 10, no. 5, pp. 52–59, 1999.

[41] J. Chaffee and J. Abel, "GDOP and the Cramer-Rao bound," in *Proceedings of 1994 IEEE Position, Location and Navigation Symposium - PLANS'94*, 1994, pp. 663–668, doi: 10.1109/PLANS.1994.303374.

[42] ETH Autonomous System Laboratory, "M100 Assembly," *github*. https://github.com/ethz-asl/dji_onboard_sdk_ros/wiki/M100-Assembly (accessed Sep. 03, 2020).

[43] T. Takasu and A. Yasuda, "Development of the low-cost RTK-GPS receiver with an open source program package RTKLIB," *Int. Symp. GPS/GNSS*, Jan. 2009.

[44] R. Opromolla, G. Inchingolo, and G. Fasano, "Airborne Visual Detection and Tracking of Cooperative UAVs Exploiting Deep Learning," *Sensors* , vol. 19, no. 19. 2019, doi: 10.3390/s19194332.

[45] P. Furgale, J. Rehder, and R. Siegwart, "Unified temporal and spatial calibration for multi-sensor systems," in *2013 IEEE/RSJ International Conference on Intelligent Robots and Systems*, 2013, pp. 1280–1286, doi: 10.1109/IROS.2013.6696514.

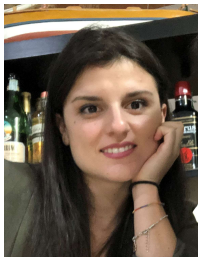

Flavia Causa received the M.S. degrees in aerospace engineering and the Ph.D. degree in Industrial Engineering from the University of Naples Federico II in 2015 and in 2020. Since 2020, she is a research fellow at University of Naples "Federico II". Her research interests include precise cooperative and distributed navigation of space platforms relying on GNSS measurement and GNC for unmanned aerial vehicles, with particular focus on cooperative navigation for small UAVs and path planning and UAV management in urban environments. She is reviewer for MDPI and IEEE journals. Miss Causa was awarded with the Amelia Earhart fellowship in 2019.

Giancarmine Fasano received the M.S. and Ph.D. degrees in Aerospace Engineering in 2004 and 2007, respectively. He is currently an Associate Professor at the University of Naples "Federico II", where he holds the courses "Unmanned Aircraft Systems" and "Space Flight Dynamics". His research activities in the field of aeronautics are focused on UAS, and in particular on Sense and Avoid and cooperative Multi-UAV Systems. In the space field he mainly works on distributed space systems and proximity operations, with emphasis on relative motion design and control.

He is Member of the IEEE AESS Avionics Systems Panel within which he chairs the UAV Committee, Associate Editor of the IEEE AESS Magazine for the UAS area of specialty, IEEE Senior Member. He has been tutorial instructor for the IEEE/AIAA Digital Avionics Systems Conference and Guest Editor of a Special Issue of the IEEE AESS Magazine dedicated to Sense and Avoid. He is also Member of the AIAA Sensor Systems and Information Fusion Technical Committee, and he has been Member of the IAA Committee on Small Satellites. He coauthored about 150 journal/conference papers and book chapters which gained several citations within the scientific literature, and is a reviewer for top-rated journals in the field of aerospace engineering and robotics.